Copy No._____

Defence Research and Development Canada
Recherche et développement pour la défense Canada

DEFENCE R&D DÉFENSE

The flow past infinite rotating cylinders at small inclinations

David Hally

Defence R&D Canada – Atlantic

Technical Memorandum
DRDC Atlantic TM 2004-274
January 2005

Canada

The flow past infinite rotating cylinders at small inclinations

David Hally

Defence R&D Canada – Atlantic

Technical Memorandum

DRDC Atlantic TM 2004-274

January 2005

105-05809/

Author

David Hally

Approved by

R. Kuwahara
Head/Signatures

Approved for release by

K. Foster
Head/Document Review Panel

© Her Majesty the Queen as represented by the Minister of National Defence, 2005

© Sa majesté la reine, représentée par le ministre de la Défense nationale, 2005

Abstract

In order to understand the effects of propeller shaft rotation on the flow into the propellers of a twin-screw ship, the DRDC Atlantic flow solver TRANSOM was used to calculate the flow around infinitely long rotating inclined cylinders at different Reynolds numbers.

The flow was solved at flow inclinations of 8°, 10° and 12°, at Reynolds numbers of 10^5, 10^6 and 10^7 based on shaft diameter, and at nine different rotation rates. The velocity fields for all 81 cases are displayed and the primary flow features and their dependence on shaft inclination, Reynolds number and rotation rate are discussed.

Résumé

Afin de comprendre les effets de la rotation d'un arbre porte-hélice sur l'écoulement de l'eau dans les hélices d'un navire à deux hélices, le résolveur d'écoulement TRANSOM de RDDC Atlantique a servi à calculer l'écoulement autour de cylindres inclinés tournants de longueur infinie, en fonction de divers nombres de Reynolds.

L'écoulement a été résolu à des angles d'inclinaison d'écoulement respectifs de 8°, 10° et 12°, à des nombres de Reynolds respectifs de 10^5, 10^6 et 10^7 en se fondant sur le diamètre de l'arbre porte-hélice et à divers régimes de rotation. On y traite des champs de vitesses des 81 cas sont affichés, ainsi que des fonctions principales d'écoulement primaire et de leur dépendance sur l'angle d'inclinaison des arbres porte-hélice, des nombres de Reynolds et des régimes de rotation.

This page intentionally left blank.

Executive summary

The flow past infinite rotating cylinders at small inclinations

David Hally; DRDC Atlantic TM 2004-274; Defence R&D Canada – Atlantic; January 2005.

Background

The flow into a propeller significantly affects the extent to which it cavitates and, therefore, the amount of noise it radiates to the far field. On twin screw ships, a significant feature of the propeller inflow is the wake of the propeller shaft. The study reported in this document is part of an attempt to understand the effects of shaft rotation on the propeller inflow, and hence on the radiated noise of the ship.

Principal results

The DRDC Atlantic flow solver TRANSOM was used to calculate the flow around infinitely long rotating inclined cylinders at different Reynolds numbers. The flow was solved at flow inclinations of 8°, 10° and 12°, values typical of the angle at which a propeller shaft exits from the hull of a twin screw ship. The Reynolds number based on shaft diameter had values of 10^5, 10^6 and 10^7, covering the range from model scale to a full scale ship. Nine different rotation rates were used covering the range of typical values for ships. The velocity fields for all 81 cases are displayed and the primary flow features and their dependence on shaft inclination, Reynolds number and rotation rate are discussed.

Significance of results

This is the limit of an infinitely long propeller shaft; therefore it supplies the limiting inflow for the case when the shaft is very long and the propeller disk is far from the hull. Although the infinite cylinder assumption neglects the important effects of the interaction of the shaft with the hull boundary layer, it allows one to gain physical insight into the effects of the rotation on the wake. The results show that rotation has an important effect on the location and shape of the shaft wake.

Sommaire

The flow past infinite rotating cylinders at small inclinations

David Hally; DRDC Atlantic TM 2004-274; R & D pour la défense Canada – Atlantique; janvier 2005.

Contexte

L'écoulement de l'eau autour d'un arbre porte-hélice a une influence importante sur le niveau de cavitation, et donc sur le niveau de bruit transmis par rayonnement dans un champ éloigné. Sur les navires à deux hélices, une caractéristique importante du débit entrant dans l'hélice est le sillage de l'arbre porte-hélice. L'étude mentionnée dans le présent document fait partie d'une tentative de comprendre les effets de la rotation d'un arbre sur le débit entrant dans une hélice, et donc sur le bruit que le navire transmet par rayonnement.

Résultats principaux

Le résolveur d'écoulement TRANSOM de RDDC Atlantique a servi à calculer l'écoulement autour de cylindres inclinés tournants de longueur infinie, en fonction de divers nombres de Reynolds. L'écoulement a été résolu à des angles d'inclinaison d'écoulement respectifs de 8°, 10° et 12°, ces valeurs étant représentatives de l'angle auquel un arbre porte-hélice émerge de la coque d'un navire à deux hélices. Le nombre de Reynolds se fondant sur le diamètre de l'arbre porte-hélice avait des valeurs respectives de 10^5, 10^6 et 10^7, ce qui couvrait une plage de valeurs allant d'un modèle à l'échelle à un navire pleine grandeur. On a eu recours à neuf régimes de rotation, couvrant la plage de valeurs typique pour des navires. Les champs de vitesses dans les 81 cas sont affichés, et on y traite des caractéristiques principales d'écoulement, ainsi que de leur dépendance sur l'inclinaison de l'arbre porte-hélice, le nombre de Reynolds et le régime de rotation.

Portée des résultats

Il s'agit de la limite d'un arbre porte-hélice de longueur infinie ; par conséquent, elle fournit le flux d'entrée limite dans le cas d'un arbre porte-hélice très long et où le cercle formé par l'hélice se trouve très loin de la coque. Bien que l'hypothèse du cylindre de longueur infinie néglige les effets importants de l'interaction entre l'arbre porte-hélice et la couche limite de la coque, elle permet d'obtenir un aperçu des effets de la rotation sur le sillage. Les résultats démontrent que la rotation a un effet important sur la position et la forme du sillage de l'arbre porte-hélice.

Table of contents

Abstract i

Résumé i

Executive summary iii

Sommaire iv

Table of contents v

List of figures vi

1 Introduction 1

2 Theory of the flow around an inclined infinite cylinder 3

3 The calculations 4

3.1 The grid 4

3.2 The outer boundary 4

4 Results of calculations 8

4.1 The flow field 8

4.1.1 Variation with rotation rate 8

4.1.2 Variation with inclination 10

4.1.3 Variation with Reynolds number 12

4.2 Forces 14

5 Grid dependency study 16

6 Concluding remarks 17

References 18

Annex A: Displays of results 19

Notation 47

List of figures

Figure 1: The flow geometry: side view. 2

Figure 2: The flow geometry: end view. 2

Figure 3: The circulation parameter, γ, as a function of r: $\Omega = 1.0$, $\beta = 10°$, $R_e = 10^5$. 6

Figure 4: Streamlines at different rotation rates: $\beta = 12°$, $R_e = 10^5$. 8

Figure 5: Streamlines for the flow with $\Omega = 0.1$, $\beta = 12°$ and $R_e = 10^5$. . . 9

Figure 6: Variation of the five main critical points with shaft inclination: $R_e = 10^5$ 11

Figure 7: Variation of the five main critical points with Reynolds number: $\beta = 10°$ 13

Figure 8: Comparison of the wake scaled using the PIF method: $\Omega = 0.8$, $\beta = 10°$. 13

Figure 9: The side force coefficient, C_F, as a function of Ω_c. 15

Figure 10: Variation of the drag coefficient with grid size: $\Omega = 0$, $\beta = 8°$, $R_e = 10^7$. 16

Figure 11: Variation of the radius of the stagnation point with grid size: $\Omega = 1$, $\beta = 10°$, $R_e = 10^7$. 16

Figure A.1: Shaft wake: $R_e = 10^5$; $\Omega = 0.0$; $\beta = 8°$ 20

Figure A.2: Shaft wake: $R_e = 10^6$; $\Omega = 0.0$; $\beta = 8°$ 20

Figure A.3: Shaft wake: $R_e = 10^7$; $\Omega = 0.0$; $\beta = 8°$ 20

Figure A.4: Shaft wake: $R_e = 10^5$; $\Omega = 0.1$; $\beta = 8°$ 21

Figure A.5: Shaft wake: $R_e = 10^6$; $\Omega = 0.1$; $\beta = 8°$ 21

Figure A.6: Shaft wake: $R_e = 10^7$; $\Omega = 0.1$; $\beta = 8°$ 21

Figure A.7: Shaft wake: $R_e = 10^5$; $\Omega = 0.2$; $\beta = 8°$ 22

Figure A.8: Shaft wake: $R_e = 10^6$; $\Omega = 0.2$; $\beta = 8°$ 22

Figure A.9: Shaft wake: $R_e = 10^7$; $\Omega = 0.2$; $\beta = 8^\circ$ 22
Figure A.10: Shaft wake: $R_e = 10^5$; $\Omega = 0.4$; $\beta = 8^\circ$ 23
Figure A.11: Shaft wake: $R_e = 10^6$; $\Omega = 0.4$; $\beta = 8^\circ$ 23
Figure A.12: Shaft wake: $R_e = 10^7$; $\Omega = 0.4$; $\beta = 8^\circ$ 23
Figure A.13: Shaft wake: $R_e = 10^5$; $\Omega = 0.6$; $\beta = 8^\circ$ 24
Figure A.14: Shaft wake: $R_e = 10^6$; $\Omega = 0.6$; $\beta = 8^\circ$ 24
Figure A.15: Shaft wake: $R_e = 10^7$; $\Omega = 0.6$; $\beta = 8^\circ$ 24
Figure A.16: Shaft wake: $R_e = 10^5$; $\Omega = 0.8$; $\beta = 8^\circ$ 25
Figure A.17: Shaft wake: $R_e = 10^6$; $\Omega = 0.8$; $\beta = 8^\circ$ 25
Figure A.18: Shaft wake: $R_e = 10^7$; $\Omega = 0.8$; $\beta = 8^\circ$ 25
Figure A.19: Shaft wake: $R_e = 10^5$; $\Omega = 1.0$; $\beta = 8^\circ$ 26
Figure A.20: Shaft wake: $R_e = 10^6$; $\Omega = 1.0$; $\beta = 8^\circ$ 26
Figure A.21: Shaft wake: $R_e = 10^7$; $\Omega = 1.0$; $\beta = 8^\circ$ 26
Figure A.22: Shaft wake: $R_e = 10^5$; $\Omega = 1.5$; $\beta = 8^\circ$ 27
Figure A.23: Shaft wake: $R_e = 10^6$; $\Omega = 1.5$; $\beta = 8^\circ$ 27
Figure A.24: Shaft wake: $R_e = 10^7$; $\Omega = 1.5$; $\beta = 8^\circ$ 27
Figure A.25: Shaft wake: $R_e = 10^5$; $\Omega = 2.0$; $\beta = 8^\circ$ 28
Figure A.26: Shaft wake: $R_e = 10^6$; $\Omega = 2.0$; $\beta = 8^\circ$ 28
Figure A.27: Shaft wake: $R_e = 10^7$; $\Omega = 2.0$; $\beta = 8^\circ$ 28
Figure A.28: Shaft wake: $R_e = 10^5$; $\Omega = 0.0$; $\beta = 10^\circ$ 29
Figure A.29: Shaft wake: $R_e = 10^6$; $\Omega = 0.0$; $\beta = 10^\circ$ 29
Figure A.30: Shaft wake: $R_e = 10^7$; $\Omega = 0.0$; $\beta = 10^\circ$ 29
Figure A.31: Shaft wake: $R_e = 10^5$; $\Omega = 0.1$; $\beta = 10^\circ$ 30

Figure A.32: Shaft wake: $R_e = 10^6$; $\Omega = 0.1$; $\beta = 10^\circ$ 30
Figure A.33: Shaft wake: $R_e = 10^7$; $\Omega = 0.1$; $\beta = 10^\circ$ 30
Figure A.34: Shaft wake: $R_e = 10^5$; $\Omega = 0.2$; $\beta = 10^\circ$ 31
Figure A.35: Shaft wake: $R_e = 10^6$; $\Omega = 0.2$; $\beta = 10^\circ$ 31
Figure A.36: Shaft wake: $R_e = 10^7$; $\Omega = 0.2$; $\beta = 10^\circ$ 31
Figure A.37: Shaft wake: $R_e = 10^5$; $\Omega = 0.4$; $\beta = 10^\circ$ 32
Figure A.38: Shaft wake: $R_e = 10^6$; $\Omega = 0.4$; $\beta = 10^\circ$ 32
Figure A.39: Shaft wake: $R_e = 10^7$; $\Omega = 0.4$; $\beta = 10^\circ$ 32
Figure A.40: Shaft wake: $R_e = 10^5$; $\Omega = 0.6$; $\beta = 10^\circ$ 33
Figure A.41: Shaft wake: $R_e = 10^6$; $\Omega = 0.6$; $\beta = 10^\circ$ 33
Figure A.42: Shaft wake: $R_e = 10^7$; $\Omega = 0.6$; $\beta = 10^\circ$ 33
Figure A.43: Shaft wake: $R_e = 10^5$; $\Omega = 0.8$; $\beta = 10^\circ$ 34
Figure A.44: Shaft wake: $R_e = 10^6$; $\Omega = 0.8$; $\beta = 10^\circ$ 34
Figure A.45: Shaft wake: $R_e = 10^7$; $\Omega = 0.8$; $\beta = 10^\circ$ 34
Figure A.46: Shaft wake: $R_e = 10^5$; $\Omega = 1.0$; $\beta = 10^\circ$ 35
Figure A.47: Shaft wake: $R_e = 10^6$; $\Omega = 1.0$; $\beta = 10^\circ$ 35
Figure A.48: Shaft wake: $R_e = 10^7$; $\Omega = 1.0$; $\beta = 10^\circ$ 35
Figure A.49: Shaft wake: $R_e = 10^5$; $\Omega = 1.5$; $\beta = 10^\circ$ 36
Figure A.50: Shaft wake: $R_e = 10^6$; $\Omega = 1.5$; $\beta = 10^\circ$ 36
Figure A.51: Shaft wake: $R_e = 10^7$; $\Omega = 1.5$; $\beta = 10^\circ$ 36
Figure A.52: Shaft wake: $R_e = 10^5$; $\Omega = 2.0$; $\beta = 10^\circ$ 37
Figure A.53: Shaft wake: $R_e = 10^6$; $\Omega = 2.0$; $\beta = 10^\circ$ 37
Figure A.54: Shaft wake: $R_e = 10^7$; $\Omega = 2.0$; $\beta = 10^\circ$ 37

Figure A.55: Shaft wake: $R_e = 10^5$; $\Omega = 0.0$; $\beta = 12^\circ$ 38
Figure A.56: Shaft wake: $R_e = 10^6$; $\Omega = 0.0$; $\beta = 12^\circ$ 38
Figure A.57: Shaft wake: $R_e = 10^7$; $\Omega = 0.0$; $\beta = 12^\circ$ 38
Figure A.58: Shaft wake: $R_e = 10^5$; $\Omega = 0.1$; $\beta = 12^\circ$ 39
Figure A.59: Shaft wake: $R_e = 10^6$; $\Omega = 0.1$; $\beta = 12^\circ$ 39
Figure A.60: Shaft wake: $R_e = 10^7$; $\Omega = 0.1$; $\beta = 12^\circ$ 39
Figure A.61: Shaft wake: $R_e = 10^5$; $\Omega = 0.2$; $\beta = 12^\circ$ 40
Figure A.62: Shaft wake: $R_e = 10^6$; $\Omega = 0.2$; $\beta = 12^\circ$ 40
Figure A.63: Shaft wake: $R_e = 10^7$; $\Omega = 0.2$; $\beta = 12^\circ$ 40
Figure A.64: Shaft wake: $R_e = 10^5$; $\Omega = 0.4$; $\beta = 12^\circ$ 41
Figure A.65: Shaft wake: $R_e = 10^6$; $\Omega = 0.4$; $\beta = 12^\circ$ 41
Figure A.66: Shaft wake: $R_e = 10^7$; $\Omega = 0.4$; $\beta = 12^\circ$ 41
Figure A.67: Shaft wake: $R_e = 10^5$; $\Omega = 0.6$; $\beta = 12^\circ$ 42
Figure A.68: Shaft wake: $R_e = 10^6$; $\Omega = 0.6$; $\beta = 12^\circ$ 42
Figure A.69: Shaft wake: $R_e = 10^7$; $\Omega = 0.6$; $\beta = 12^\circ$ 42
Figure A.70: Shaft wake: $R_e = 10^5$; $\Omega = 0.8$; $\beta = 12^\circ$ 43
Figure A.71: Shaft wake: $R_e = 10^6$; $\Omega = 0.8$; $\beta = 12^\circ$ 43
Figure A.72: Shaft wake: $R_e = 10^7$; $\Omega = 0.8$; $\beta = 12^\circ$ 43
Figure A.73: Shaft wake: $R_e = 10^5$; $\Omega = 1.0$; $\beta = 12^\circ$ 44
Figure A.74: Shaft wake: $R_e = 10^6$; $\Omega = 1.0$; $\beta = 12^\circ$ 44
Figure A.75: Shaft wake: $R_e = 10^7$; $\Omega = 1.0$; $\beta = 12^\circ$ 44
Figure A.76: Shaft wake: $R_e = 10^5$; $\Omega = 1.5$; $\beta = 12^\circ$ 45
Figure A.77: Shaft wake: $R_e = 10^6$; $\Omega = 1.5$; $\beta = 12^\circ$ 45

Figure A.78: Shaft wake: $R_e = 10^7$; $\Omega = 1.5$; $\beta = 12°$ 45

Figure A.79: Shaft wake: $R_e = 10^5$; $\Omega = 2.0$; $\beta = 12°$ 46

Figure A.80: Shaft wake: $R_e = 10^6$; $\Omega = 2.0$; $\beta = 12°$ 46

Figure A.81: Shaft wake: $R_e = 10^7$; $\Omega = 2.0$; $\beta = 12°$ 46

1 Introduction

The flow into a propeller significantly affects the extent to which it cavitates and, therefore, the amount of noise it radiates to the far field. On twin screw ships, a significant feature of the propeller inflow is the wake of the propeller shaft. The study reported in this document is part of an attempt to understand the effects of shaft rotation on the propeller inflow, and hence on the radiated noise of the ship.

The DRDC Atlantic flow solver TRANSOM[1] was used to calculate the flow around infinitely long rotating inclined cylinders at different Reynolds numbers. This is the limit of an infinitely long propeller shaft; therefore it supplies the limiting inflow for the case when the shaft is very long and the propeller disk is far from the hull. Although the infinite cylinder assumption neglects the important effects of the interaction of the shaft with the hull boundary layer[2], it allows one to gain physical insight into the effects of the rotation on the wake. Moreover, due to the symmetry of the infinite cylinder approximation, the numerical calculations can be performed on a two-dimensional grid; they do not require large amounts of computer time. Therefore a large number of cases can be calculated to determine the most important effects on the wake.

The flow was solved at three different flow inclinations, three different Reynolds numbers, and nine different rotation rates: 81 cases in all (the geometry of the flow is shown in Figures 1 and 2). The flow inclination, β, had values of 8°, 10° and 12°, typical of the angle with which a propeller shaft leaves the hull of a twin screw ship.

The Reynolds number based on shaft diameter, R_e, had values of 10^5, 10^6 and 10^7, roughly spanning the range from model scale to full scale ship (a ship with shafts of 0.5 metre diameter steaming at 30 knots has $R_e = 8 \times 10^6$; a 1/20 Froude scaled model of the same ship has $R_e = 9 \times 10^4$).

Rotation rate is quantified using the non-dimensional parameter Ω, defined by

$$\Omega = \frac{\omega R_s}{V_\infty} \tag{1}$$

where ω is the angular velocity of the shaft, R_s is the shaft radius, and V_∞ is the speed of inflow. Therefore Ω is the speed of the fluid at the the shaft surface relative to the speed of inflow. For a ship the rotation parameter can be related to the advance coefficient, J, by

$$\Omega = \frac{\pi}{J}\frac{R_s}{R_p} \tag{2}$$

where R_p is the radius of the propeller. For a ship, typical values for Ω are in the range 0.5 to 1.0. The nine values used in the flow calculations were 0.0, 0.1, 0.2, 0.4, 0.6, 0.8, 1.0, 1.5 and 2.0.

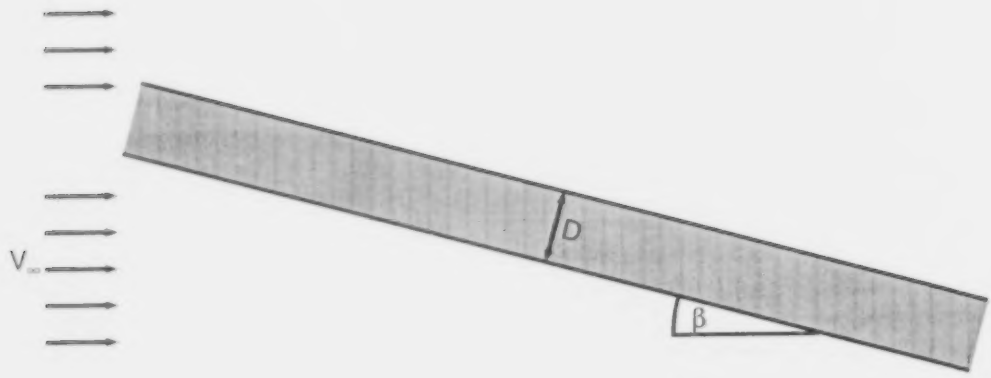

Figure 1: *The flow geometry: side view.*

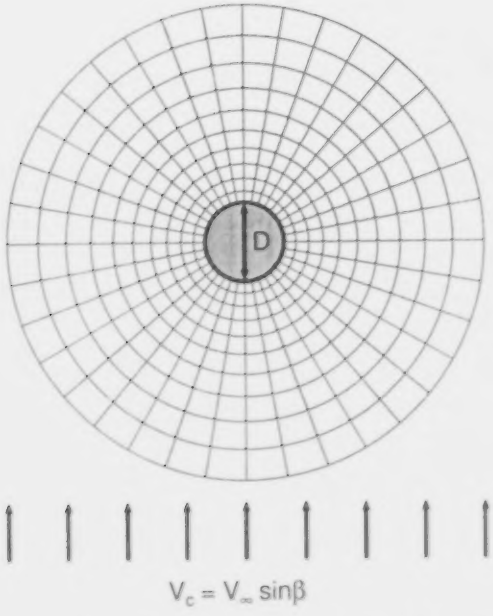

Figure 2: *The flow geometry: end view. The topology of the grid is also shown. V_c is the cross-flow velocity.*

2 Theory of the flow around an inclined infinite cylinder

We use a Cartesian coordinate system in which the z axis is aligned with the cylinder. Since the cylinder is infinite and the flow steady, the is no variation of the velocity or pressure in the z direction. The equations of motion for the flow are then:

$$\frac{\partial u}{\partial x} + \frac{\partial v}{\partial y} = 0 \tag{3}$$

$$u\frac{\partial u}{\partial x} + v\frac{\partial u}{\partial y} = -\frac{1}{\rho}\frac{\partial p}{\partial x} + \frac{\partial}{\partial x}\left(2\nu_t\frac{\partial u}{\partial x}\right) + \frac{\partial}{\partial y}\left(\nu_t\left[\frac{\partial u}{\partial y} + \frac{\partial v}{\partial x}\right]\right) \tag{4}$$

$$u\frac{\partial v}{\partial x} + v\frac{\partial v}{\partial y} = -\frac{1}{\rho}\frac{\partial p}{\partial y} + \frac{\partial}{\partial x}\left(\nu_t\left[\frac{\partial v}{\partial x} + \frac{\partial u}{\partial y}\right]\right) + \frac{\partial}{\partial y}\left(2\nu_t\frac{\partial v}{\partial y}\right) \tag{5}$$

$$u\frac{\partial w}{\partial x} + v\frac{\partial w}{\partial y} = \frac{\partial}{\partial x}\left(\nu_t\left[\frac{\partial w}{\partial x}\right]\right) + \frac{\partial}{\partial y}\left(\nu_t\left[\frac{\partial w}{\partial y}\right]\right) \tag{6}$$

where ν_t is the turbulent kinematic viscosity. Equations (3)–(5) are the equations of motion for a two-dimensional fluid. The equation for w, Equation (6), is (almost) decoupled from the equations for u and v, Equations (3)–(5), and is in the form of a convection-diffusion equation for the scalar variable w.

If the flow is laminar, then the decoupling is complete and the flow could be solved by first calculating p, u, and v, then doing a separate calculation of w. However, if the flow is turbulent, then w will effect ν_t and so will also have an effect on u and v.

The Spalart-Allmaras turbulence model[3] calculates ν_t in terms of a different kinematic viscosity variable $\tilde{\nu}$. The turbulent kinematic viscosity is given in terms of $\tilde{\nu}$ by:

$$\nu_t = \nu + \tilde{\nu} f_{v1}; \qquad f_{v1} = \frac{\chi^3}{\chi^3 + c_{v1}^3}; \qquad \chi = \frac{\tilde{\nu}}{\nu} \tag{7}$$

where ν is the laminar kinematic viscosity and c_{v1} is a constant. The following transport equation is used to calculate $\tilde{\nu}$ (all z derivatives vanish due to the infinite cylinder approximation):

$$u\frac{\partial \tilde{\nu}}{\partial x} + v\frac{\partial \tilde{\nu}}{\partial y} = \frac{1}{\sigma}\left[\frac{\partial}{\partial x}\left((\nu+\tilde{\nu})\frac{\partial \tilde{\nu}}{\partial x}\right) + \frac{\partial}{\partial y}\left((\nu+\tilde{\nu})\frac{\partial \tilde{\nu}}{\partial y}\right) + c_{b2}\left(\left(\frac{\partial \tilde{\nu}}{\partial x}\right)^2 + \left(\frac{\partial \tilde{\nu}}{\partial y}\right)^2\right)\right] + c_{b1}\tilde{S}\tilde{\nu} - c_{w1} f_w \left(\frac{\tilde{\nu}}{d}\right)^2 \tag{8}$$

with

$$\tilde{S} = |\omega| + \frac{f_{v2}\tilde{\nu}}{\kappa^2 d^2}; \qquad f_{v2} = 1 - \frac{\chi}{1+\chi f_{v1}}; \qquad f_w = g\left[\frac{1+c_{w3}^6}{g^6 + c_{w3}^6}\right]^{1/6} \tag{9}$$

$$g = r + c_{w2}(r^6 - r); \qquad r = \frac{\tilde{\nu}}{\tilde{S}\kappa^2 d^2} \tag{10}$$

and d is the distance to the nearest wall, ω is the vorticity, and c_{b1}, c_{b2}, c_{w1}, c_{w2}, c_{w3}, κ, and σ are constants. While u and v enter this equation via the convection terms, w only appears by virtue of its contribution to the vorticity magnitude. However, when the flow is nearly in the same direction as the cylinder, as in the case of a propeller shaft, w will be an order of magnitude larger than u and v and the gradient of w will be the dominant contribution to the vorticity magnitude close to the shaft. Therefore, the effect of w on the distribution of u and v will be significant.

The DRDC Atlantic flow solver TRANSOM can be used to calculate the flow past an infinite cylinder. TRANSOM solves Equations (3)–(5) for p, u and v, then solves Equation (6) for w, and finally solves Equation (9) for $\tilde{\nu}$. This procedure is repeated until the maximum residuals have been reduced sufficiently.

3 The calculations

TRANSOM was used to calculate the flow at inclinations of 8°, 10° and 12°, at Reynolds numbers of 10^5, 10^6 and 10^7 based on shaft diameter, and at rotation rates, $\Omega = 0.0$, 0.1, 0.2 0.4, 0.5 0.8, 1.0, 1.5 and 2.0.

3.1 The grid

The calculations were performed on a grid using a simple O topology around the cylinder: see Figure 2. The 361 nodes around the circumference of the cylinder were equally spaced. The 201 nodes in the radial direction followed a geometric distribution such that the distance of the nearest nodes to the shaft surface was $3 \times 10^{-6} D$, where D is the cylinder diameter. This results in y^+ values of the order of 1.0 for the largest Reynolds number of 10^7.

3.2 The outer boundary

The rotation of the shaft induces a net circulation around it. The circulation $\kappa(r)$ around a circle of radius r centred on the shaft axis is

$$\kappa(r) = \int_0^{2\pi} v_\theta(r, \theta) r \, d\theta \tag{11}$$

Define a circulation coefficient by

$$\gamma(r) = \frac{\kappa}{2\pi R_s} \tag{12}$$

The circulation coefficient $\gamma(r)$ has units of velocity; it is equivalent to the velocity on the surface of the shaft if the circulation at r were induced by a Rankine vortex. If the flow were purely potential, the circulation coefficient would be constant. However, due to the boundary layer of the shaft, the circulation coefficient drops rapidly as r first increases from R_s; it approaches a constant once r is greater than a few shaft diameters.

The circumferential velocity, v_θ, associated with the circulation falls off slowly as $1/r$. Therefore it is necessary to choose an outer boundary that is far enough from the shaft that the interaction of the rotation with the outer boundary will not induce significant errors near the shaft. Suppose that a free-stream boundary condition is used over the outer boundary; that is, on the inflow portion of the outer boundary the velocity is set to $\mathbf{V} = \hat{z}V_\infty \cos\beta + \hat{y}V_\infty \sin\beta$, where $\hat{z}$ is the axial direction and $\hat{y}$ is the vertical direction; on the outflow portion of the outer boundary the pressure is set to zero. Since there is no contribution to the circulation from the inflow portion of the outer boundary, we can estimate the effect of the interaction of the outer boundary with the shaft rotation by using the analytical solution for the rotating flow between two concentric circular cylinders, the inner cylinder rotating with angular velocity ω and the outer cylinder stationary. The solution for this flow is (for example, see Batchelor[4, page 202])

$$v_\theta = \frac{\omega R_s^2}{R_o^2 - R_s^2}\left(\frac{R_o^2}{r} - r\right) \tag{13}$$

where R_o is the radius at the outer boundary. The circulation coefficient for this flow is

$$\gamma(r) = \omega R_s \frac{R_o^2 - r^2}{R_o^2 - R_s^2} \tag{14}$$

Thus, γ drops off quadratically from ωR_s at the shaft surface, to zero at the outer boundary.

If $R_o \longrightarrow \infty$, the solution is

$$v_\theta = \frac{\omega R_s^2}{r} \tag{15}$$

Therefore, the difference between the solution with R_o finite and R_o infinite is:

$$\Delta v_\theta = \frac{\omega R_s^2}{R_o^2 - R_s^2}\left(\frac{R_s^2}{r} - r\right) \tag{16}$$

This represents the velocity induced by the finite outer boundary. It is a strictly increasing function for $r > R_s$. If we wish the induced velocity to be less than a fraction, ϵ, of the upwash due to the shaft inclination over the whole propeller disk, then we must have

$$\left|\frac{\omega R_s^2}{R_o^2 - R_s^2}\left(\frac{R_s^2}{R_p} - R_p\right)\right| < \epsilon V_\infty \sin\beta \tag{17}$$

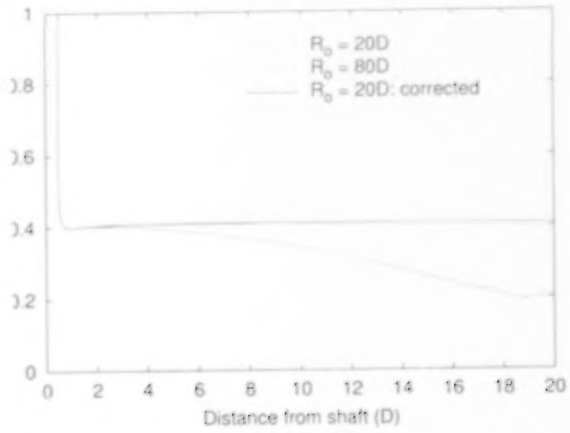

Figure 3: *The circulation parameter, γ, as a function of r: $\Omega = 1.0$, $\beta = 10°$, $R_e = 10^7$. The curves labelled 20D and 80D have uniform inflow at outer boundaries of $20D$ and $80D$. The curve labelled 20D: corrected has the corrected outer boundary at $20D$.*

where R_p is the radius of the propeller disk. Therefore

$$\frac{R_o}{R_s} > \sqrt{1 + \frac{|\Omega|}{\epsilon \sin\beta}\left(\frac{R_p}{R_s} - \frac{R_s}{R_p}\right)} \tag{18}$$

With $R_p/R_s = 3$, $\Omega = 2$, $\epsilon = 0.01$ and $\beta = 8°$, we have $R_o > 62D$.

Rather than increasing R_o, a different approach was taken. The radius R_o was fixed at $20D$, but to avoid the problem described above, the flow was calculated in two steps. First it was calculated using free stream boundary conditions on the outer boundary. This solution is sufficiently accurate near the shaft that it provides a good estimate of the circulation, $\gamma(R_o)$, induced by the rotation. Once the circulation is known, the flow is solved again with the outer boundary conditions set to match the potential flow past a cylinder with rotating rate set to generate the correct circulation. The resulting flow is accurate throughout the domain.

Figure 3 shows the circulation coefficient calculated from solutions for which $R_o = 20D$ and $80D$ and whose outer boundaries used free stream boundary conditions; also shown is the circulation when $R_o = 20D$ but the corrected potential flow boundary condition was used. The circulation coefficient with $R_o = 20D$ and free-stream boundary conditions falls off quadratically for large r. It does not fall all the way to zero because circulation is precluded only on the inflowing portion of the boundary. When $R_o = 80D$, the circulation is nearly constant between $r = 2D$ and $20D$, but

Table 1: *Circulation coefficient, $\gamma(R_o)$, used to correct the flow near the outer boundary*

$\beta = 8°$									
	Ω								
R_e	0.0	0.1	0.2	0.4	0.6	0.8	1.0	1.5	2.0
10^5	0.0000	0.0417	0.0873	0.1880	0.2472	0.2990	0.3647	0.5416	0.6854
10^6	0.0000	0.0445	0.0914	0.1945	0.2456	0.2866	0.3415	0.5042	0.6338
10^7	0.0000	0.0476	0.0963	0.1997	0.2446	0.2778	0.3236	0.4757	0.5941

$\beta = 10°$									
	Ω								
R_e	0.0	0.1	0.2	0.4	0.6	0.8	1.0	1.5	2.0
10^5	0.0000	0.0418	0.0869	0.1921	0.2760	0.3354	0.4025	0.6050	0.7667
10^6	0.0000	0.0451	0.0925	0.1977	0.2800	0.3279	0.3818	0.5661	0.7116
10^7	0.0000	0.0486	0.0985	0.2034	0.2834	0.3226	0.3661	0.5354	0.6694

$\beta = 12°$									
	Ω								
R_e	0.0	0.1	0.2	0.4	0.6	0.8	1.0	1.5	2.0
10^5	0.0000	0.0411	0.0854	0.1888	0.2930	0.3646	0.4320	0.6568	0.8362
10^6	0.0000	0.0440	0.0924	0.1956	0.3012	0.3636	0.4175	0.6193	0.7797
10^7	0.0000	0.0489	0.0993	0.2036	0.3086	0.3629	0.4064	0.5881	0.7362

at the higher radii it begins to decrease slowly; as r increases past $20D$ it does fall off quadratically to a value near 0.2 at $r = 80D$, though this is not shown in Figure 3. The circulation coefficient when the corrected boundary condition is used is also nearly constant over the range $2D$ to $20D$.

Table 1 gives the circulation coefficient used to correct the outer boundary condition for each of the runs.

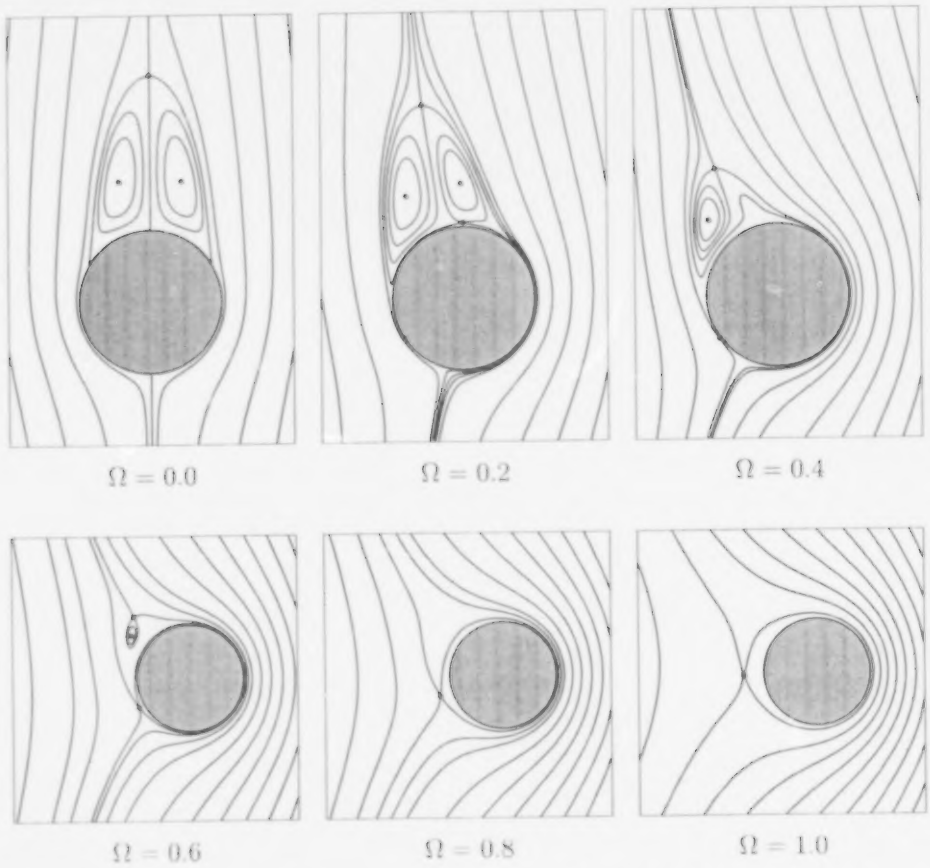

Figure 4: *Streamlines at different rotation rates: $\beta = 12°$, $R_e = 10^5$. The critical points are marked by the blue dots.*

4 Results of calculations

4.1 The flow field

The results of all the calculations performed on the medium grid are displayed in Annex A. In the following sections the primary effects on the flow of shaft inclination, rotation and Reynolds number are discussed.

4.1.1 Variation with rotation rate

The inclination of the shaft causes an upward flow across the shaft of $V_\infty \sin\beta$. When there is no rotation (see Figures A.1–A.3, A.28–A.30 and A.55–A.57), the flow is similar to the flow across a cylinder. The axial wake has a region of velocity deficit

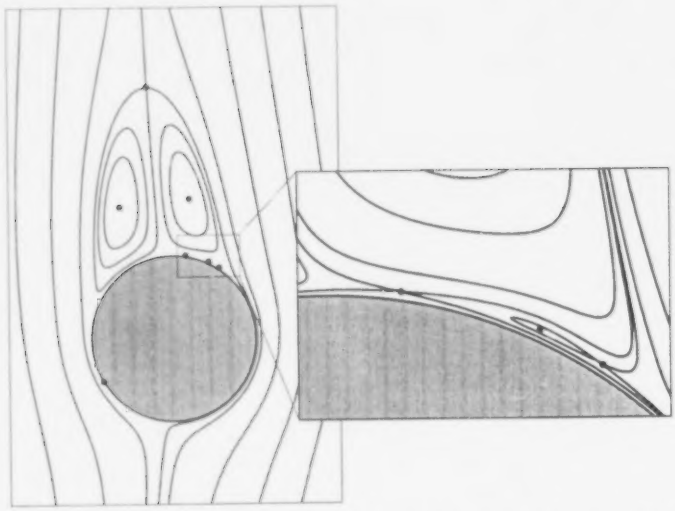

Figure 5: *Streamlines for the flow with $\Omega = 0.1$, $\beta = 12°$ and $R_e = 10^5$. The critical points are marked by the blue dots. The expanded region shows the small third vortex.*

directly above the shaft. The flow separates from the shaft near two o'clock and ten o'clock, and two counter-rotating vortices form in the lee of the shaft. As well as the complete shaft surface, there are three points in the flow where the tangential velocity vanishes (critical points): the centres of the two vortices, and a stagnation point on the centreline ($x = 0$) which marks the upper limit of the circulation bubbles associated with the vortices: see Figure 4.

When the shaft is rotating, the tangential velocity at its surface no longer vanishes. Instead, two new stagnation points are introduced just off the surface near eight o'clock and twelve o'clock (we assume in this discussion that the rotation is counter-clockwise: positive Ω). The centres of the vortices both move to the left and the upper stagnation point moves toward the shaft. The axial wake also rotates counterclockwise around the shaft and assumes a slightly bowed shape. This is due to the convection of the axial wake by both the circulation induced by the shaft rotation and by the cross-flow due to the shaft inclination.

As the rotation rate increases, both vortices decrease in size, but the right vortex does so faster than the left. For Ω near 0.1, the right stagnation point splits into two as a very small third vortex, rotating clockwise, appears beneath the right vortex: see Figure 5. This vortex seems to be present for only a small range of rotation rates. In our runs it only appeared for the case $\Omega = 0.1$ with $\beta = 10°$ and $12°$. Since such low rotations are not of importance for ship propellers, the details of this flow feature have not be pursued further.

Table 2: *Variation with rotation rate and Reynolds number of the vorticity at the centre of the two major vortices: $\beta = 10°$. The vorticity has been non-dimensionalized using the shaft diameter, D, and the free-stream velocity, V_∞.*

	left vortex			right vortex		
Ω	$R_e = 10^5$	$R_e = 10^6$	$R_e = 10^7$	$R_e = 10^5$	$R_e = 10^6$	$R_e = 10^7$
0.0	-0.3334	-0.3669	-0.3999	0.3333	0.3668	0.3998
0.1	-0.3434	-0.3751	-0.4057	0.3262	0.3594	0.3907
0.2	-0.3532	-0.3820	-0.4085	0.3057	0.3314	0.3575
0.4	-0.3493	-0.3497	-0.3558			

The right vortex disappears when Ω is between 0.2 and 0.4 (later for higher shaft inclinations). Finally, when Ω is between 0.4 and 0.8 the left vortex also disappears. When the vortices have disappeared the axial wake becomes somewhat thinner. It then thickens again slowly as Ω continues to increase: for example, see Figures A.19, A.22 and A.25.

The axial wake continues to rotate counterclockwise as Ω increases. Once Ω is much larger than 1.0, the wake leaves the shaft near nine o'clock. The only significant change in the axial wake as Ω increases further is its continued thickening.

Table 2 gives the vorticity at the centre of each of the two major vortices. As the rotation rate increases, the right vortex diminishes in strength: the left vortex increases in strength, then between $\Omega = 0.2$ and 0.4, begins to decrease until it disappears.

When the vortices have disappeared, the lower left stagnation point is the only remaining critical point. So far it has stayed close to the shaft surface, but it now begins to move leftward into the flow. It continues to do so as the rotation rate increases.

Figure 6 shows how the locations of the five main critical points change with rotation rate and shaft inclination.

4.1.2 Variation with inclination

For all the calculations, the flow far from the shaft wake approximates very closely the potential flow around the shaft with equivalent circulation. Therefore, far from the shaft wake, the axial flow is a near uniform $V_\infty \cos \beta$. For two cases with the same shaft inclination, the variation in the tangential flow field far from the shaft wake is due solely to the variation of the induced circulation with β: see Table 1.

Figure 6 shows how the five main critical points vary with rotation rate and shaft inclination. The upper stagnation point moves farther from the shaft as the shaft

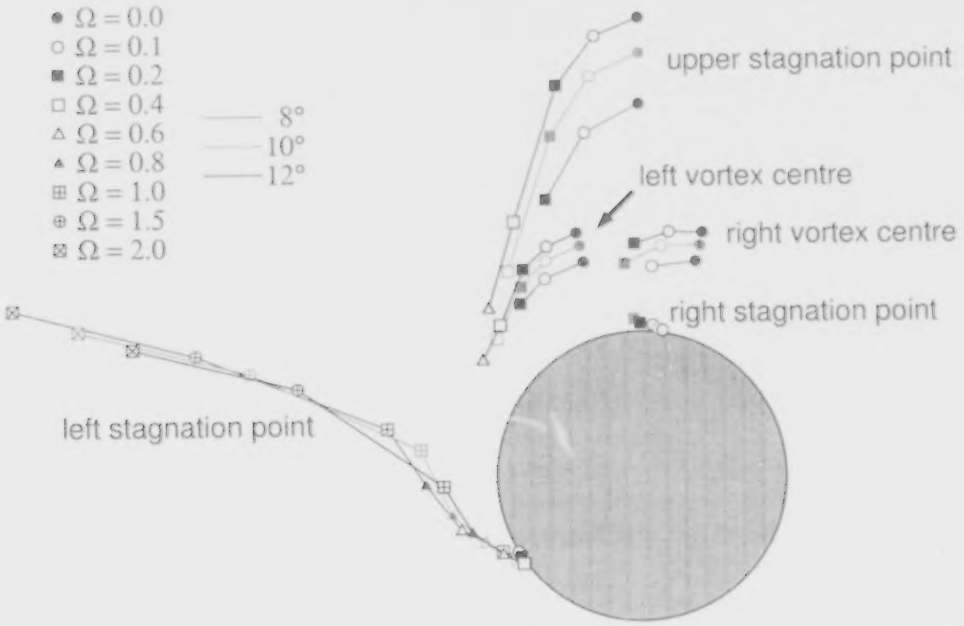

Figure 6: *Variation of the five main critical points with shaft inclination:* $R_e = 10^5$

inclination increases: i.e. the separation bubble around the vortices is longer for higher inclinations. The centres of the vortices also move away from the shaft as the inclination increases.

Table 3 gives the vorticity at the centre of each of the two major vortices at different rotation rates and shaft inclinations; the Reynolds number is fixed at 10^5. As expected, since the cross-flow increases with β, the strengths of the vortices also increase with β. This also results in the vortices persisting to higher rotation rates.

The lower left stagnation point is the location where the cross-flow and the rotation induced circulation just cancel one another. As β increases, the cross-flow also increases so the stagnation point moves closer to the shaft where the velocities induced by the circulation are also higher. At low rotation rates the stagnation point is very close to the cylinder. Here the gradient in the circulation induced velocity is very high, so the location of the stagnation point varies very little with rotation. At higher rotation rates the stagnation point moves away from the cylinder where the gradient in the circulation induced velocity is low; the location of the stagnation point is then quite sensitive to the inclination angle.

The counterclockwise rotation of the axial wake is reduced as β increases though the effect is fairly small: for example, see Figures A.18, A.45 and A.72. The amount

Table 3: *Variation with rotation rate and shaft inclination of the vorticity at the centre of the two major vortices: $R_e = 10^5$. The vorticity has been non-dimensionalized using the shaft diameter, D, and the free-stream velocity, V_∞.*

	left vortex			right vortex		
Ω	$\beta = 8°$	$\beta = 10°$	$\beta = 12°$	$\beta = 8°$	$\beta = 10°$	$\beta = 12°$
0.0	-0.2618	-0.3333	-0.3995	0.2618	0.3333	0.3994
0.1	-0.2740	-0.3434	-0.4048	0.2353	0.3262	0.4019
0.2	-0.2707	-0.3532	-0.4196		0.3057	0.4050
0.4		-0.3493	-0.4448			
0.6			-0.4235			

of wake rotation depends on the relative importance of convection by the induced circulation and convection by the cross-flow. At higher shaft inclinations the latter becomes more important and the wake rotation is reduced slightly.

For Ω above 0.4, the axial wake becomes a little thinner and a little deeper (i.e. the velocity deficit is slightly larger) as β increases: for example, see Figures A.26, A.53 and A.80.

4.1.3 Variation with Reynolds number

Figure 7 shows how the five main critical points vary with rotation rate and Reynolds number. The upper stagnation point moves closer to the shaft as the Reynolds number increases: i.e. the separation bubble around the vortices is shorter for higher Reynolds numbers. The centres of the vortices also move closer to the shaft as the Reynolds number increases.

Table 2 shows that the strength of the vortices increases with Reynolds number. This suggests that for higher Reynolds numbers the vortices may persist to slightly higher rotation rates; however, the number of different rotation rates used is not sufficient to determine whether this is actually true.

As the Reynolds number increases, the velocity deficit in the axial wake decreases due to the reduced production of velocity deficit at the shaft surface. The location of the wake is nearly independent of the Reynolds number; this is of importance to empirical wake scaling methods which assume that the location of the wake does not vary with Reynolds number.

The wake scaling method developed by the Co-operative Research Ships Propeller Inflow (PIF) Working Group[5] has been used to scale the wake with $\Omega = 0.8$ and

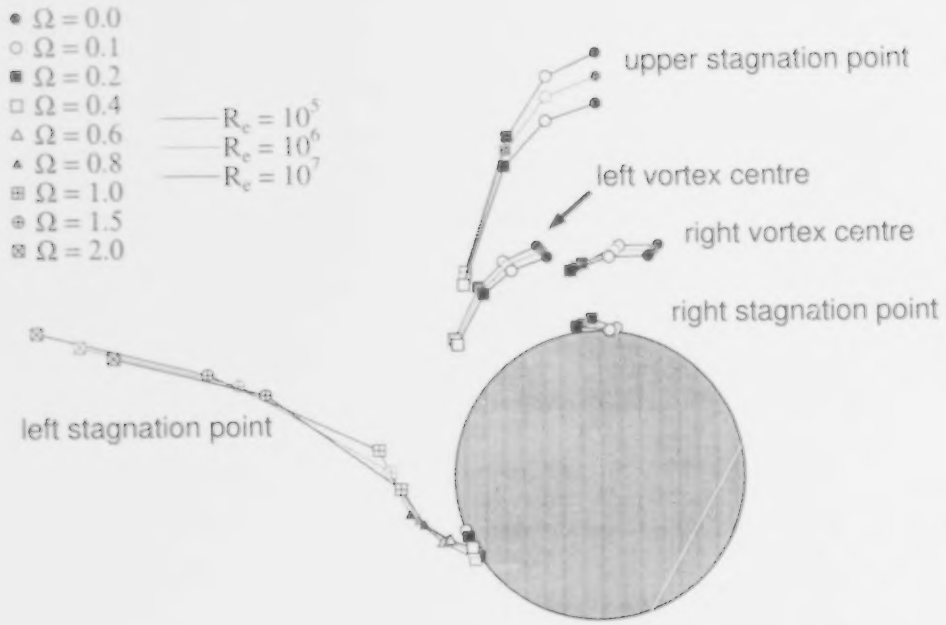

Figure 7: *Variation of the five main critical points with Reynolds number:* $\beta = 10^{\circ}$

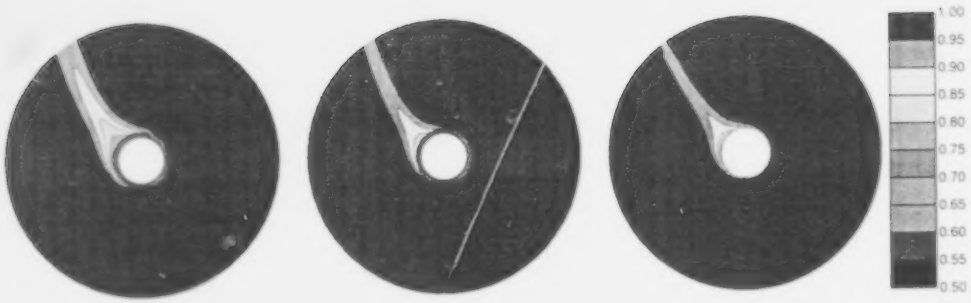

$R_e = 10^5$ $R_e = 10^7$ $R_e = 10^7$ scaled

Figure 8: *Comparison of the wake scaled using the PIF method:* $\Omega = 0.8$, $\beta = 10^{\circ}$.

$\beta = 10°$ from $R_e = 10^5$ to $R_e = 10^7$. Figure 8 shows the wake with $R_e = 10^5$, the wake with $R_e = 10^7$ in the middle, and the wake scaled from $R_e = 10^5$ to $R_e = 10^7$ on the right. The scaled wake shows reasonable agreement with the calculated wake at $R_e = 10^7$. The velocity deficit is slightly underpredicted in the scaled wake. The scaled wake is also a little bit straighter than the calculated wake. This is probably because the method contracts the wake toward the mean wake centre along a line with constant θ. Since the wake is curved, it is not being contracted toward the center of the wake.

4.2 Forces

The forces on the shaft were calculated by integrating the pressure and the viscous stress over the surface of the shaft. The drag varied significantly between the calculations with free-stream outer boundary conditions and the potential flow outer boundary conditions. This appears to be due to a small rotation (of the order of a few degrees) in the streamlines caused by the imposition of the outer flow (see Section 3.2). If we denote the side force by F_x and the drag force by F_y, and the small rotation angle by ϕ, then the effect of the rotation on the side force is roughly

$$F_x \longrightarrow F_x \cos\phi + F_y \sin\phi \approx F_x + F_y \sin\phi \tag{19}$$

For typical rotation rates the drag is much smaller than the side force. Since $\sin\phi$ is also small, the net effect on the side force is negligible. However the effect of the streamline rotation on the drag is roughly

$$F_y \longrightarrow -F_x \sin\phi + F_y \cos\phi = F_y - F_x \sin\phi \tag{20}$$

Because F_x is typically much larger than F_y, the relative change in F_y can be appreciable. Consequently, except for the cases with no rotation, we have no confidence that the drag predictions are accurate; they will not be reported here. Instead we concentrate on the prediction of the side force, F_x.

The cross-flow velocity is

$$V_c = V_\infty \sin\beta \tag{21}$$

We define a side force coefficient by non-dimensionalizing the side force with respect to V_c:

$$C_F = \frac{-F_x}{\frac{1}{2}\rho V_\infty^2 \sin^2\beta} \tag{22}$$

Figure 9 plots the side force coefficient as a function of $\Omega_c = \Omega/\sin\beta$, the ratio of the speed at the shaft surface to the cross-flow velocity, V_c. The solid curve in Figure 9 is the lift curve for a rotating cylinder ($\beta = 90°$) measured by Ackeret as reported by

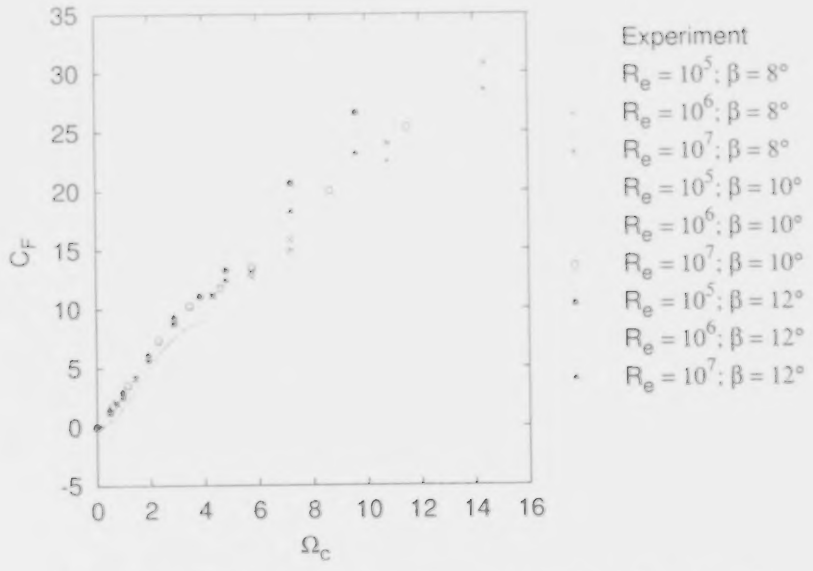

Figure 9: *The side force coefficient, C_F, as a function of Ω_c. The solid line is the side force measured for a rotating cylinder ($\beta = 90°$).*

Dodge and Thompson[6]. For small rotation rates the force coefficient collapses well onto a single curve, which is in reasonable agreement with the experimental data, given the difference in shaft inclination. For higher rotation rates, the data no longer collapses onto a single curve: the side force coefficient increases with inclination angle and decreases with Reynolds number. The mechanism involved is not understood.

Table 4: *Number of nodes in each grid*

	N_θ	N_r	N
tiny	91	51	4,641
small	181	101	18,281
medium	361	201	72,561
big	721	401	289,121

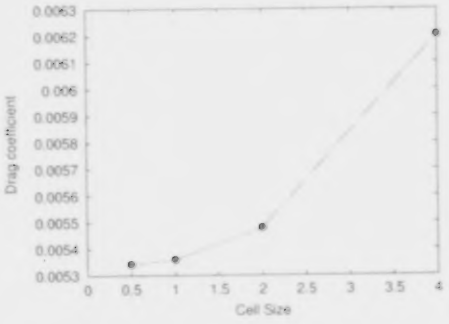

Figure 10: *Variation of the drag coefficient with grid size: $\Omega = 0$, $\beta = 8°$, $R_e = 10^7$. Cell size is relative to the medium grid.*

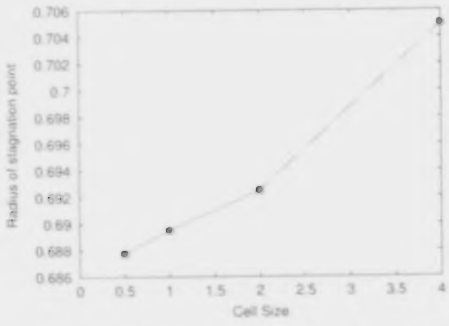

Figure 11: *Variation of the radius of the stagnation point with grid size: $\Omega = 1$, $\beta = 10°$, $R_e = 10^7$. Cell size is relative to the medium grid.*

5 Grid dependency study

The effect of the size of the grid on the calculations was measured by calculating several of the cases on a hierarchy of four grids having different node densities. The grids were denoted tiny, small, medium and big. The medium grid was the grid used in all other calculations. Each grid used a simple O topology around the cylinder. For each grid Table 4 tabulates the number of radial nodes, N_r, the number of circumferential nodes, N_θ, and the total number of nodes.

Comparisons of the results of the different grids suggests that the medium grid is large enough to yield accurate results in all cases. For example, Figure 10 shows the variation of the drag coefficient with cell size for the non-rotating case with $\beta = 8°$ and a Reynolds number of 10^7. The cell size is given relative to the medium grid therefore the big grid has cellsize of 0.5 and the tiny grid a cell size of 4. The drag coefficient converges well as the grid density increases. The difference between the drag predictions on the two finest grids is within the numerical error expected for the drag calculation.

Figure 11 shows the variation of the radius of the stagnation point when $\Omega = 1.0$, $\beta = 10°$ and the Reynolds number is 10^7. The error in the location predicted using the medium grid is too high by about 0.5%.

6 Concluding remarks

To understand better the wakes of rotating propeller shafts, the flow about infinitely long rotating cylinders at small inclinations to the free stream has been calculated using the DRDC Atlantic flow solver TRANSOM. The flow was calculated for three inclinations, three Reynolds numbers and nine rotation rates, spanning the ranges typically encountered on ships from model to full scale.

When the shaft does not rotate, the wake is confined to the region immediately above the shaft. As the shaft begins to rotate, the axial wake also rotates around the shaft until it leaves the shaft at nine o'clock (for counterclockwise shaft rotation); this occurs once the rotation rate, $\Omega = 1$, is significantly larger than 1.0. The axial wake also assumes a curved shape due to its convection by both the circulation induced by the shaft rotation and by the cross-flow induced by the shaft inclination.

The counter-rotating vortices which are present in the tangential wake for low rotation rates, disappear between $\Omega = 0.2$ and 0.4; they persist longer at higher shaft inclinations.

The primary effect of increasing the Reynolds number is to reduce the velocity deficit in the axial wake. Higher Reynolds numbers do cause the counter-rotation vortices to diminish slightly in size and increase slightly in strength.

To test its validity for the case of a rotating shaft, the PIF wake scaling method was used to scale some of the wakes from Reynolds number 10^5 to 10^7. The results were generally good, though the velocity deficit in the scaled wake was slightly underpredicted. The location of the scaled wake was also shifted slightly due to the way in which the PIF method contracts the wake.

References

1. Hally, D. (1997). TRANSOM: A Multi-method Navier-Stokes Solver: Overall Design. (DREA TM 97-231). Defence R&D Canada – Atlantic.

2. Hally, D. (2004). The Wakes of Idealized Propeller Shafts with Cross-flow and Rotation. In *Proceedings of the 25th Symposium on Naval Hydrodynamics*, St. John's, NF, Canada.

3. Spalart, P. R. and Allmaras, S. R. (1992). A One-Equation Turbulence Model for Aerodynamic Flows. Technical Report. AIAA Paper 92-0439.

4. Batchelor, G. K. (1967). An Introduction to Fluid Mechanics, Cambridge University Press.

5. Hally, D. (2002). The CRS PIF method for scaling wakes of twin screw ships. (DREA ECR 2002-051). Defence R&D Canada – Atlantic. Limited distribution.

6. Dodge, Russell A. and Thompson, Milton J. (1937). Fluid Mechanics, McGraw-Hill Book Co. Ltd., New York.

Annex A: Displays of results

This annex contains displays of the flow fields for all 81 runs. Each of the three velocity components v_z, v_r and v_θ are shown as shaded contour plots in the region $R_s \leq r \leq 3D$, roughly the size of a typical propeller disk. The direction of increasing θ is clockwise around the disk in accordance with the ITTC convention.

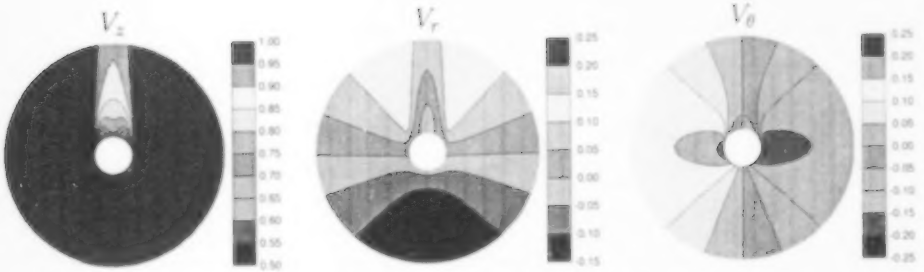

Figure A.1: *Shaft wake:* $R_e = 10^5$; $\Omega = 0.0$; $\beta = 8°$

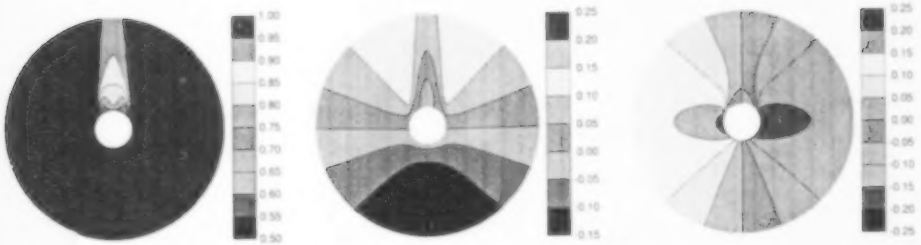

Figure A.2: *Shaft wake:* $R_e = 10^6$; $\Omega = 0.0$; $\beta = 8°$

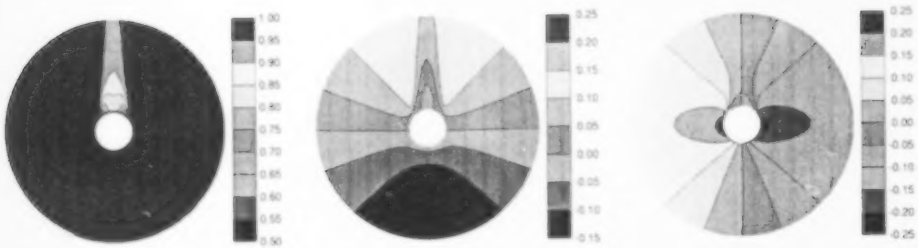

Figure A.3: *Shaft wake:* $R_e = 10^7$; $\Omega = 0.0$; $\beta = 8°$

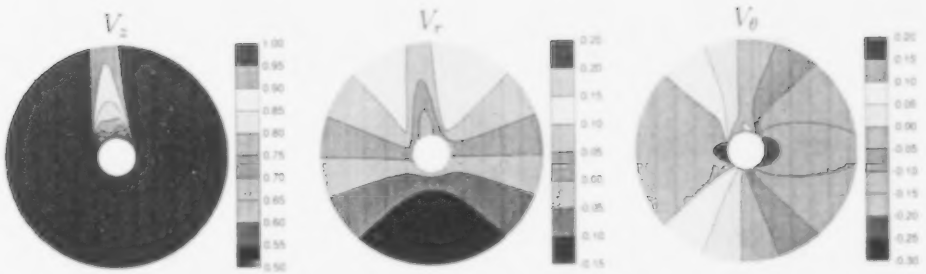

Figure A.4: *Shaft wake:* $R_e = 10^5$; $\Omega = 0.1$; $\beta = 8°$

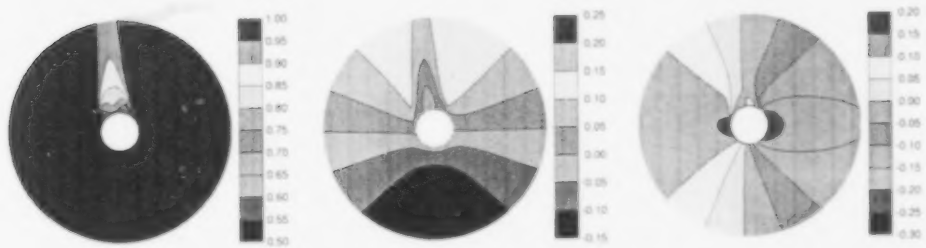

Figure A.5: *Shaft wake:* $R_e = 10^6$; $\Omega = 0.1$; $\beta = 8°$

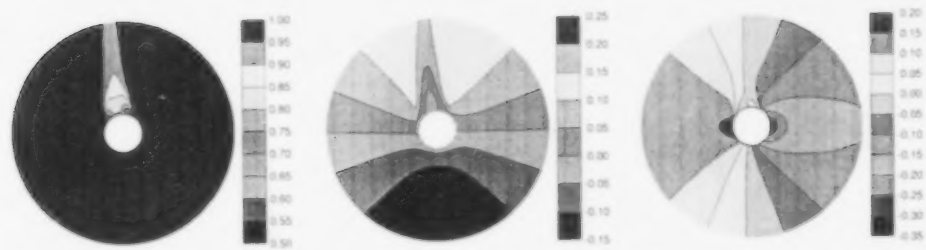

Figure A.6: *Shaft wake:* $R_e = 10^7$; $\Omega = 0.1$; $\beta = 8°$

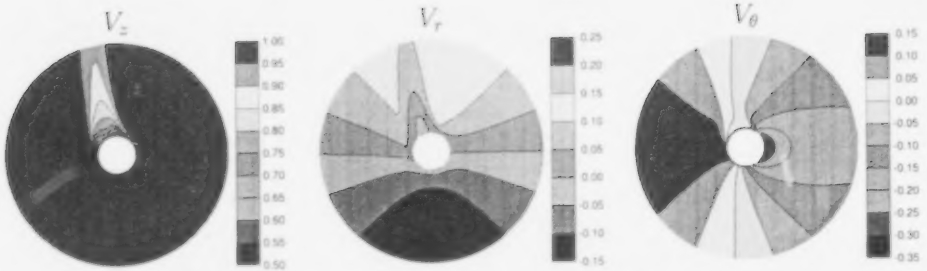

Figure A.7: *Shaft wake:* $R_e = 10^5$; $\Omega = 0.2$; $\beta = 8°$

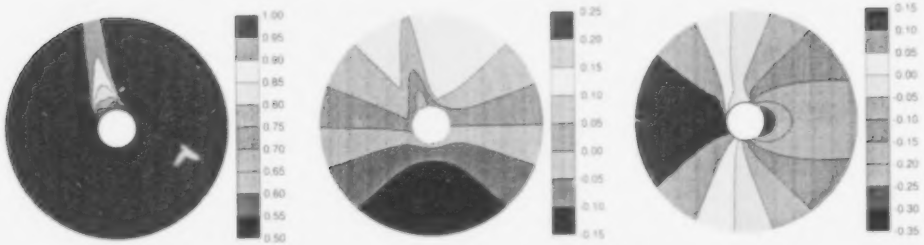

Figure A.8: *Shaft wake:* $R_e = 10^6$; $\Omega = 0.2$; $\beta = 8°$

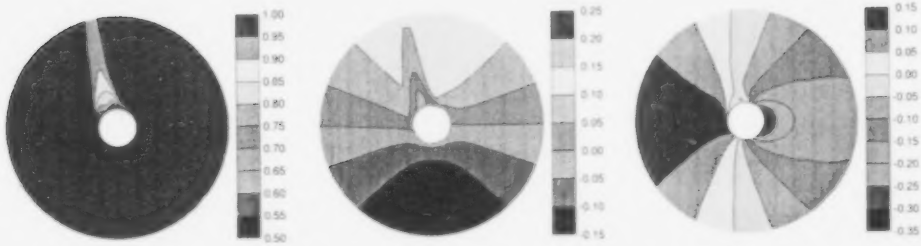

Figure A.9: *Shaft wake:* $R_e = 10^7$; $\Omega = 0.2$; $\beta = 8°$

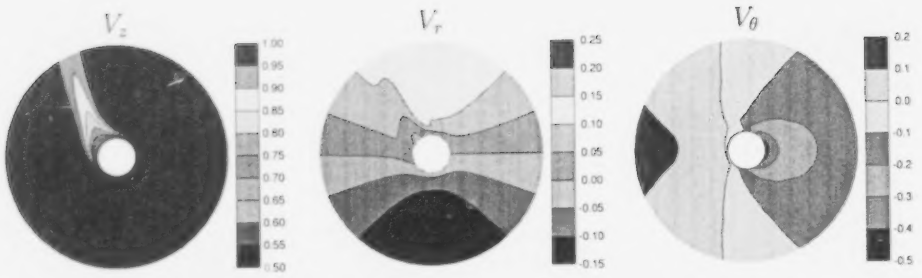

Figure A.10: *Shaft wake:* $R_e = 10^5$; $\Omega = 0.4$; $\beta = 8°$

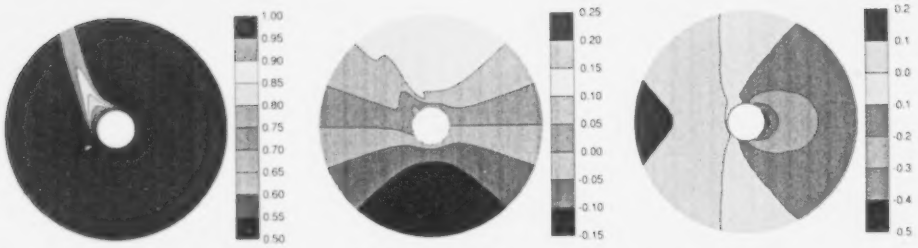

Figure A.11: *Shaft wake:* $R_e = 10^6$; $\Omega = 0.4$; $\beta = 8°$

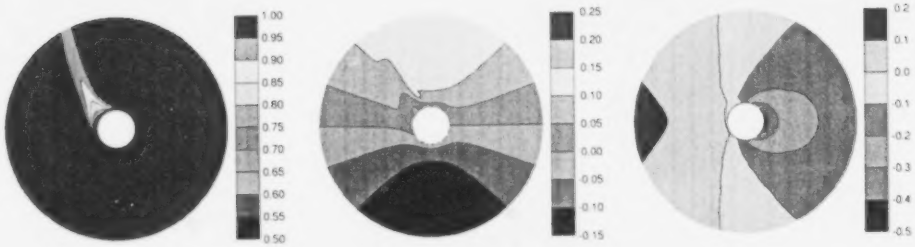

Figure A.12: *Shaft wake:* $R_e = 10^7$; $\Omega = 0.4$; $\beta = 8°$

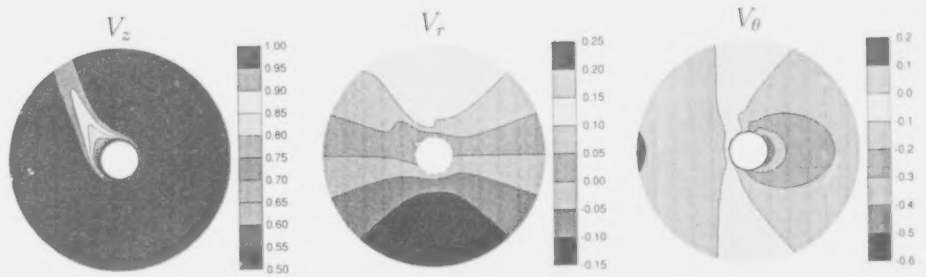

Figure A.13: *Shaft wake:* $R_e = 10^5$; $\Omega = 0.6$; $\beta = 8°$

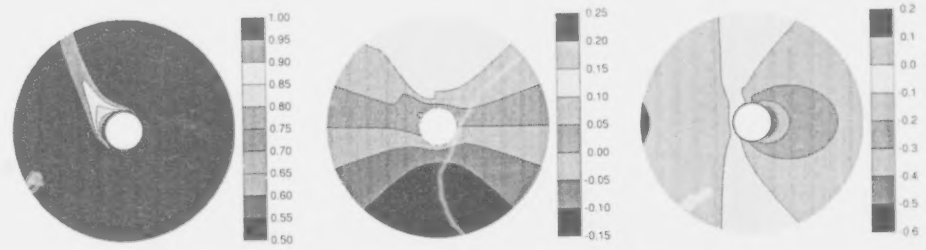

Figure A.14: *Shaft wake:* $R_e = 10^6$; $\Omega = 0.6$; $\beta = 8°$

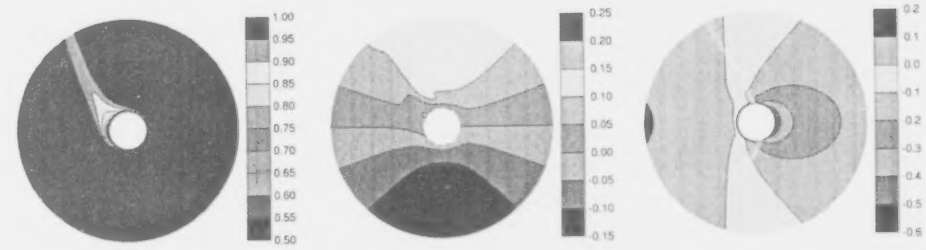

Figure A.15: *Shaft wake:* $R_e = 10^7$; $\Omega = 0.6$; $\beta = 8°$

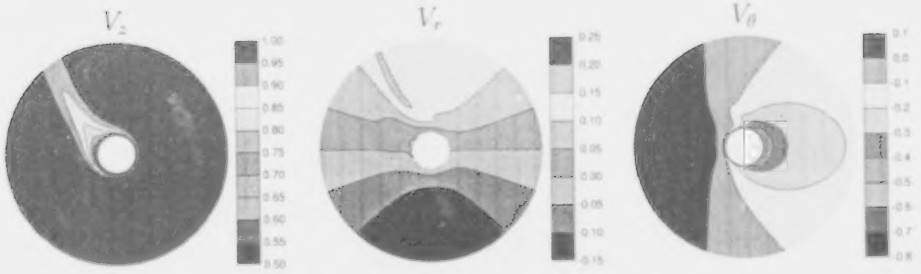

Figure A.16: *Shaft wake:* $R_e = 10^5$; $\Omega = 0.8$; $\beta = 8°$

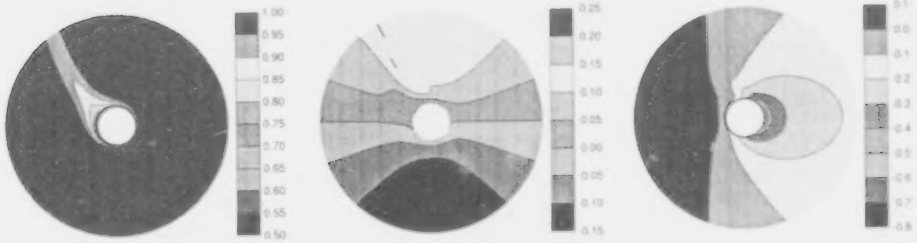

Figure A.17: *Shaft wake:* $R_e = 10^6$; $\Omega = 0.8$; $\beta = 8°$

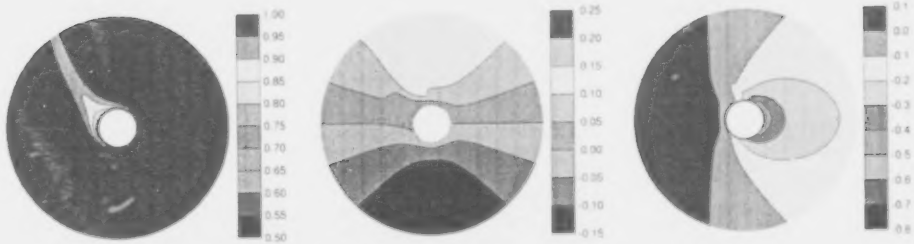

Figure A.18: *Shaft wake:* $R_e = 10^7$; $\Omega = 0.8$; $\beta = 8°$

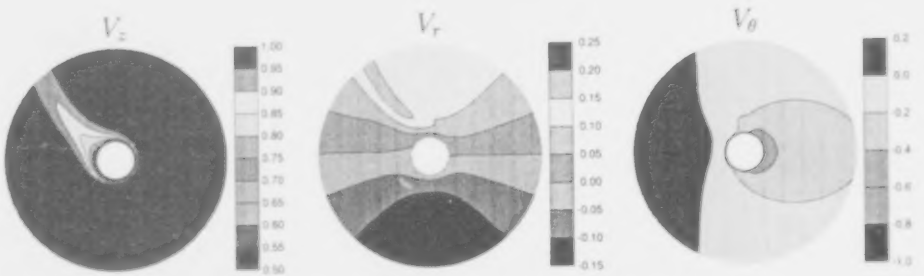

Figure A.19: *Shaft wake:* $R_e = 10^5$; $\Omega = 1.0$; $\beta = 8°$

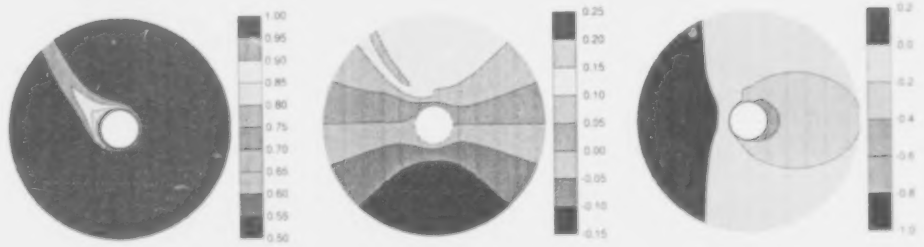

Figure A.20: *Shaft wake:* $R_e = 10^6$; $\Omega = 1.0$; $\beta = 8°$

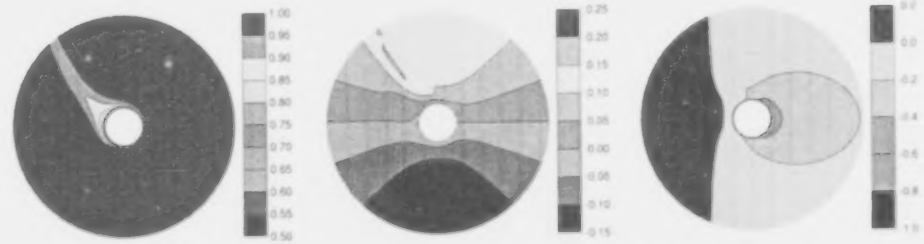

Figure A.21: *Shaft wake:* $R_e = 10^7$; $\Omega = 1.0$; $\beta = 8°$

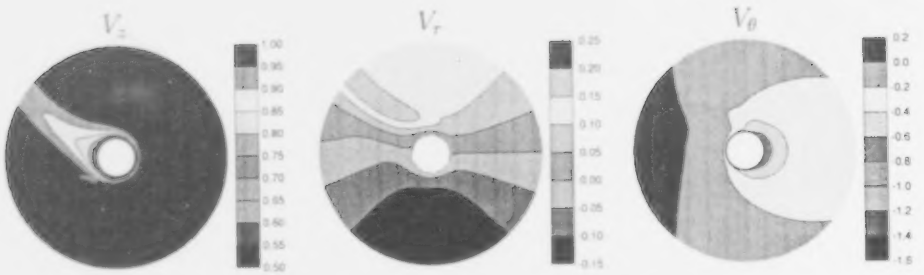

Figure A.22: *Shaft wake:* $R_e = 10^5$; $\Omega = 1.5$; $\beta = 8°$

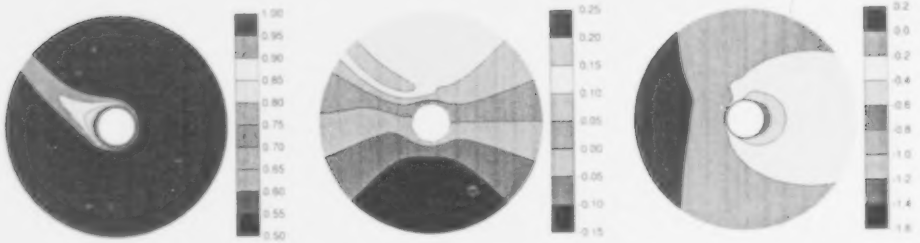

Figure A.23: *Shaft wake:* $R_e = 10^6$; $\Omega = 1.5$; $\beta = 8°$

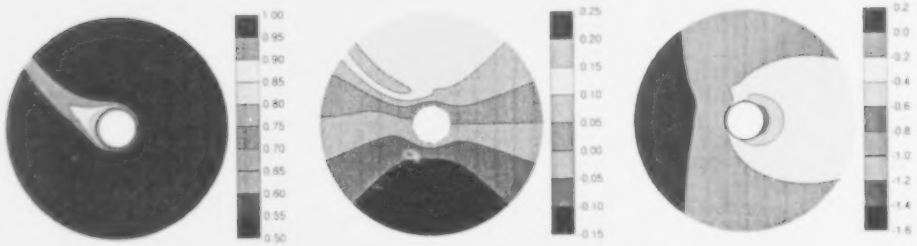

Figure A.24: *Shaft wake:* $R_e = 10^7$; $\Omega = 1.5$; $\beta = 8°$

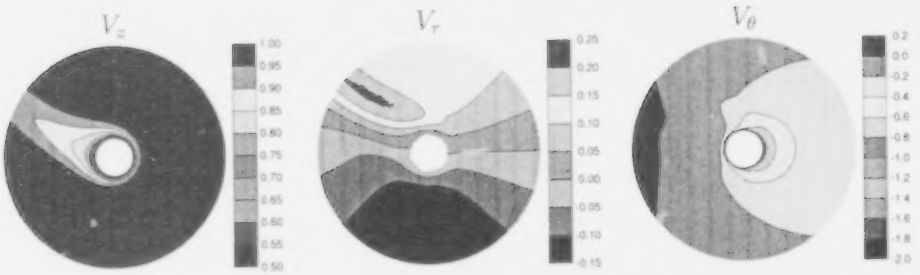

Figure A.25: *Shaft wake:* $R_e = 10^5$; $\Omega = 2.0$; $\beta = 8°$

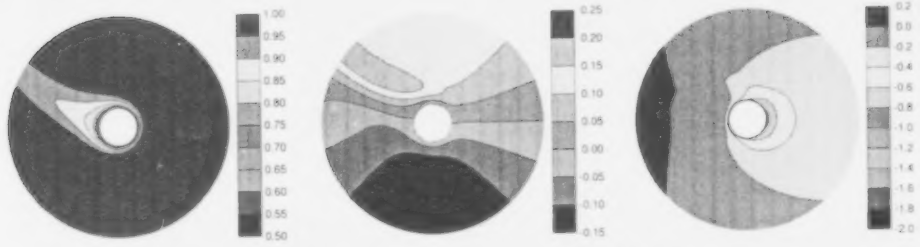

Figure A.26: *Shaft wake:* $R_e = 10^6$; $\Omega = 2.0$; $\beta = 8°$

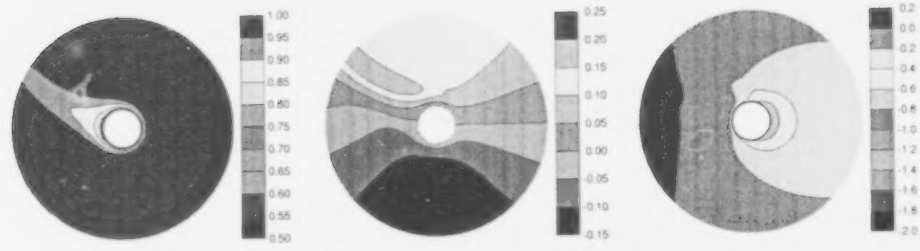

Figure A.27: *Shaft wake:* $R_e = 10^7$; $\Omega = 2.0$; $\beta = 8°$

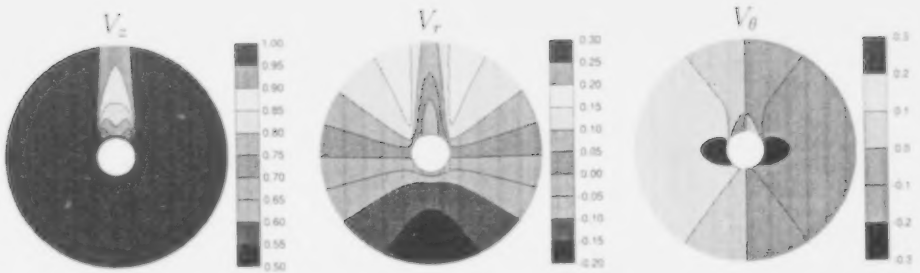

Figure A.28: *Shaft wake:* $R_e = 10^5$; $\Omega = 0.0$; $\beta = 10°$

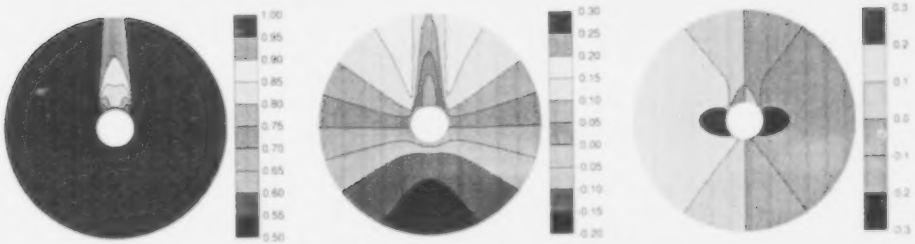

Figure A.29: *Shaft wake:* $R_e = 10^6$; $\Omega = 0.0$; $\beta = 10°$

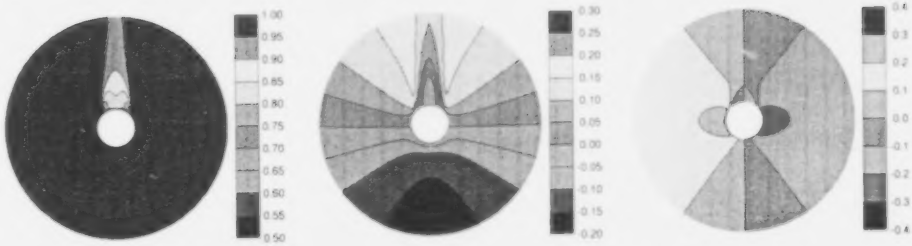

Figure A.30: *Shaft wake:* $R_e = 10^7$; $\Omega = 0.0$; $\beta = 10°$

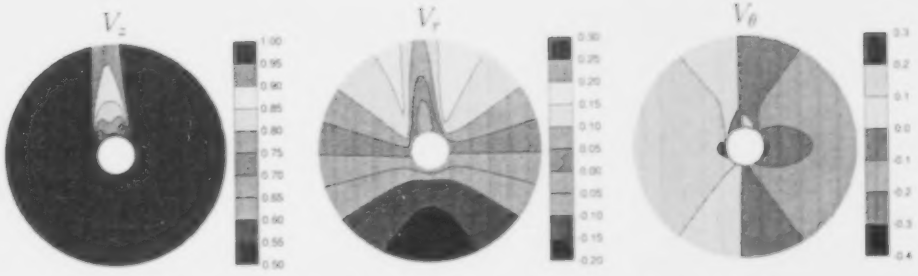

Figure A.31: *Shaft wake:* $R_e = 10^5$; $\Omega = 0.1$; $\beta = 10°$

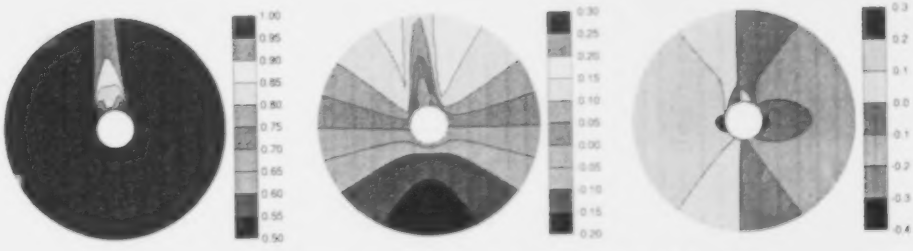

Figure A.32: *Shaft wake:* $R_e = 10^6$; $\Omega = 0.1$; $\beta = 10°$

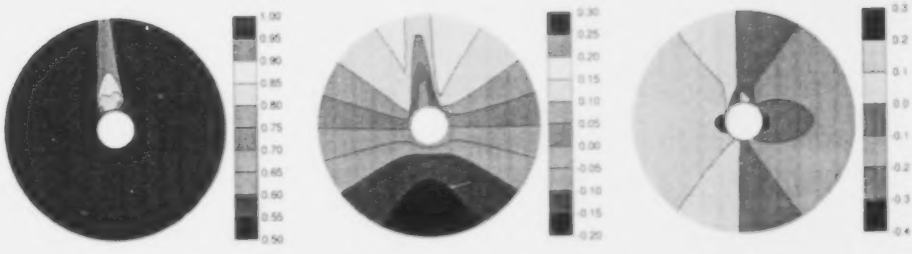

Figure A.33: *Shaft wake:* $R_e = 10^7$; $\Omega = 0.1$; $\beta = 10°$

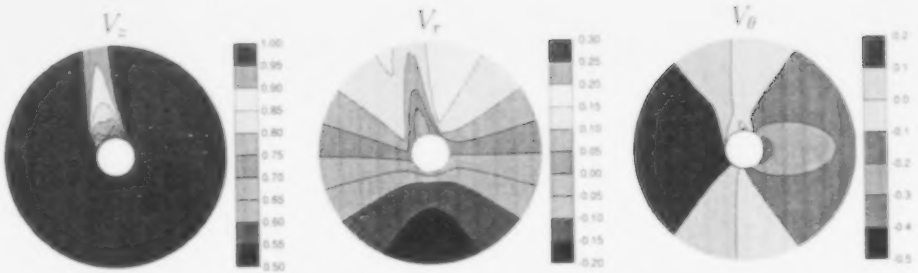

Figure A.34: *Shaft wake:* $R_e = 10^5$; $\Omega = 0.2$; $\beta = 10°$

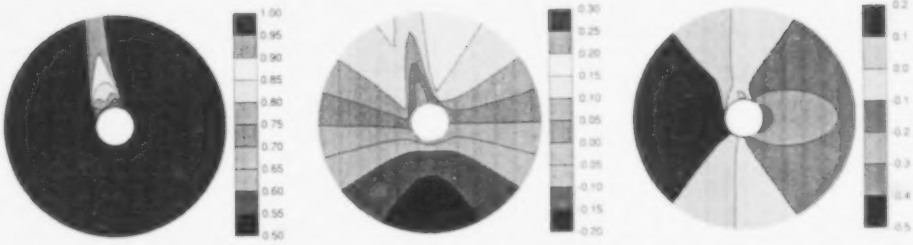

Figure A.35: *Shaft wake:* $R_e = 10^6$; $\Omega = 0.2$; $\beta = 10°$

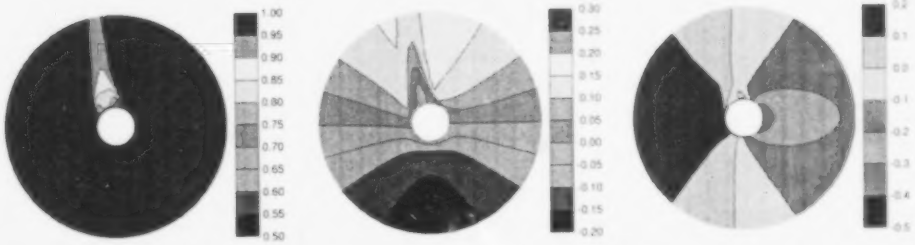

Figure A.36: *Shaft wake:* $R_e = 10^7$; $\Omega = 0.2$; $\beta = 10°$

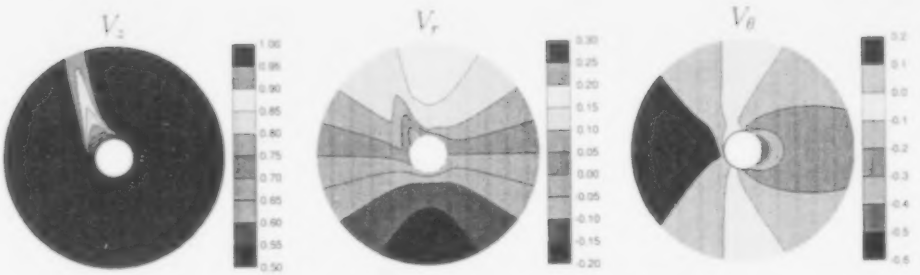

Figure A.37: *Shaft wake:* $R_e = 10^5$; $\Omega = 0.4$; $\beta = 10°$

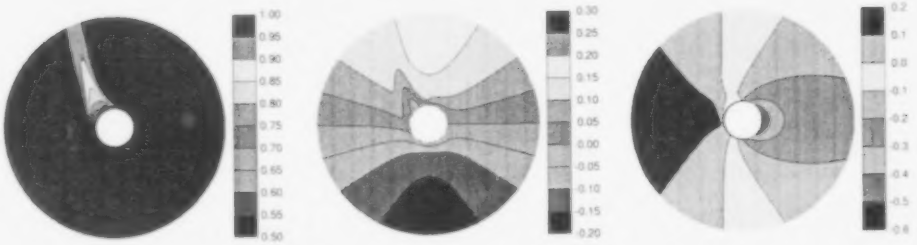

Figure A.38: *Shaft wake:* $R_e = 10^6$; $\Omega = 0.4$; $\beta = 10°$

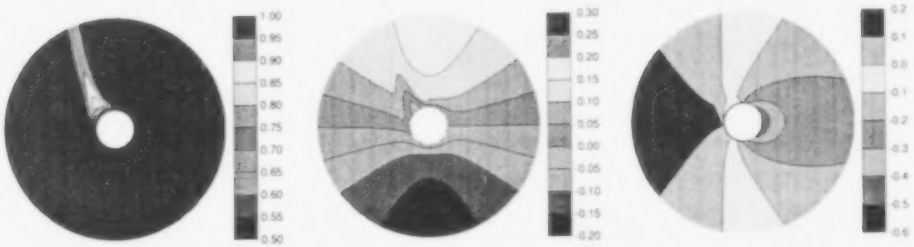

Figure A.39: *Shaft wake:* $R_e = 10^7$; $\Omega = 0.4$; $\beta = 10°$

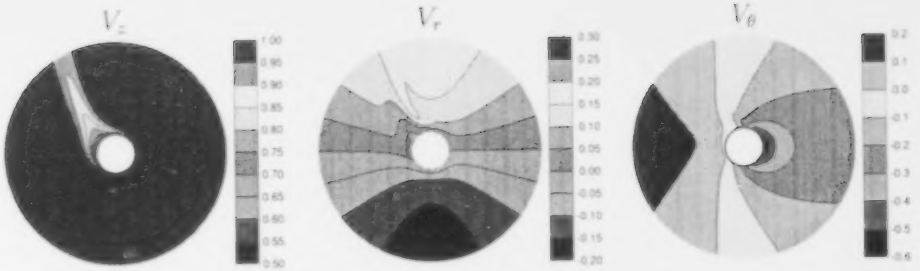

Figure A.40: *Shaft wake:* $R_e = 10^5$; $\Omega = 0.6$; $\beta = 10°$

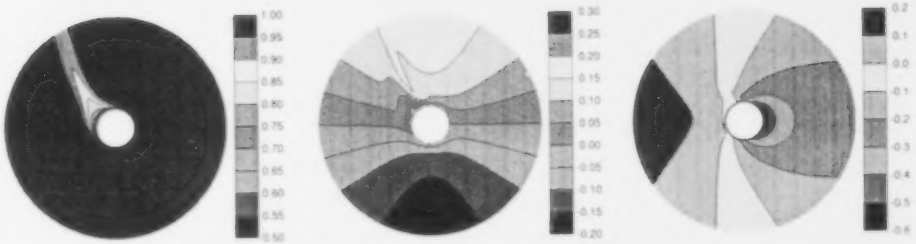

Figure A.41: *Shaft wake:* $R_e = 10^6$; $\Omega = 0.6$; $\beta = 10°$

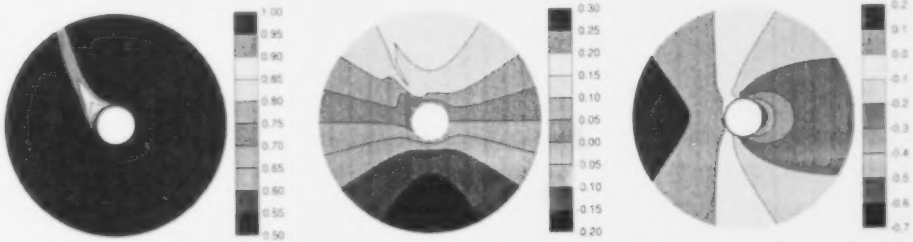

Figure A.42: *Shaft wake:* $R_e = 10^7$; $\Omega = 0.6$; $\beta = 10°$

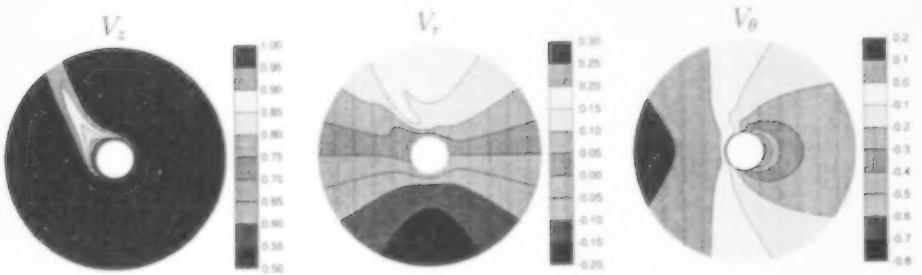

Figure A.43: *Shaft wake:* $R_e = 10^5$; $\Omega = 0.8$; $\beta = 10^\circ$

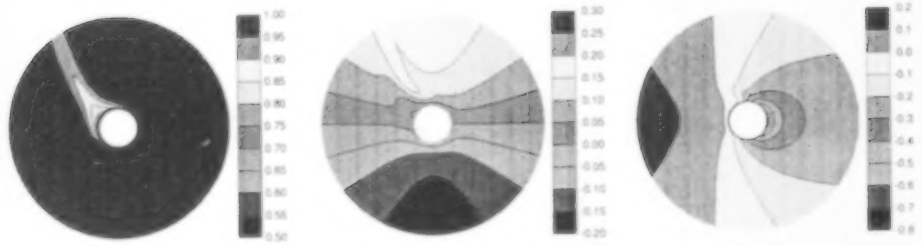

Figure A.44: *Shaft wake:* $R_e = 10^6$; $\Omega = 0.8$; $\beta = 10^\circ$

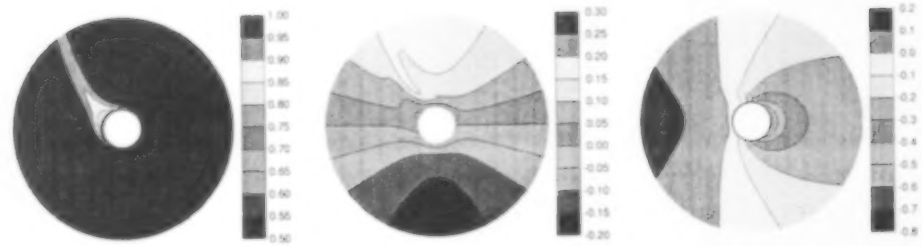

Figure A.45: *Shaft wake:* $R_e = 10^7$; $\Omega = 0.8$; $\beta = 10^\circ$

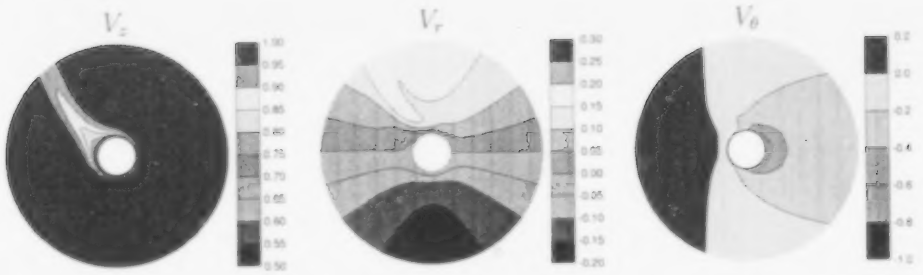

Figure A.46: *Shaft wake:* $R_e = 10^5$; $\Omega = 1.0$; $\beta = 10°$

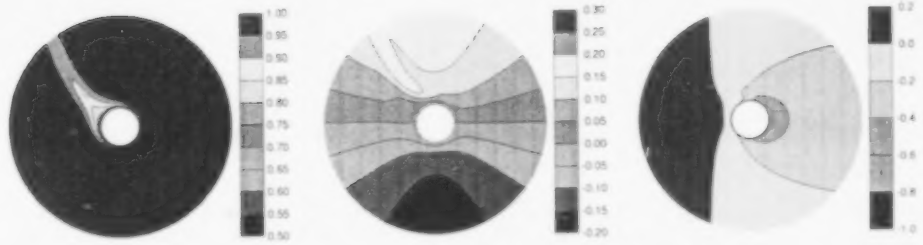

Figure A.47: *Shaft wake:* $R_e = 10^6$; $\Omega = 1.0$; $\beta = 10°$

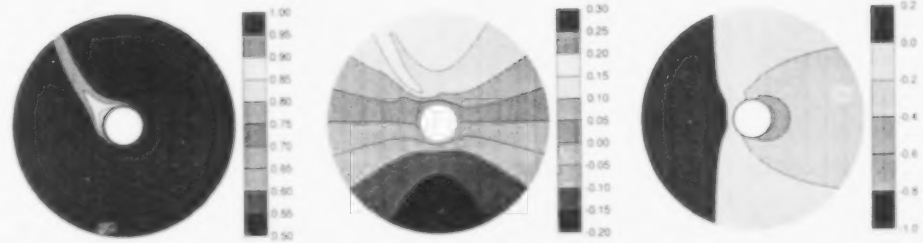

Figure A.48: *Shaft wake:* $R_e = 10^7$; $\Omega = 1.0$; $\beta = 10°$

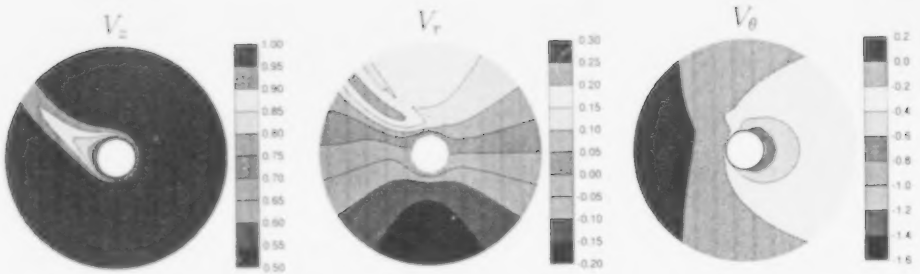

Figure A.49: *Shaft wake:* $R_e = 10^5$; $\Omega = 1.5$; $\beta = 10°$

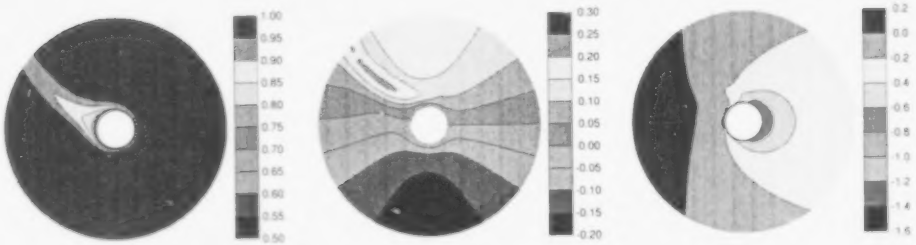

Figure A.50: *Shaft wake:* $R_e = 10^6$; $\Omega = 1.5$; $\beta = 10°$

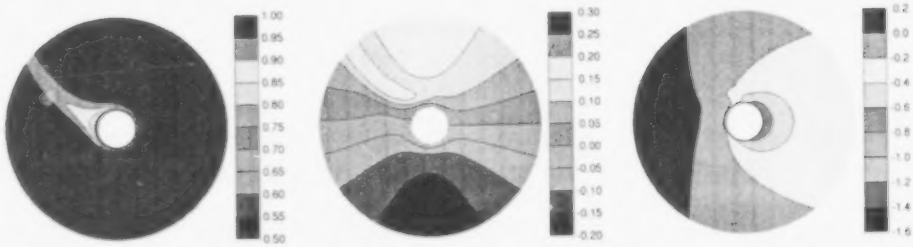

Figure A.51: *Shaft wake:* $R_e = 10^7$; $\Omega = 1.5$; $\beta = 10°$

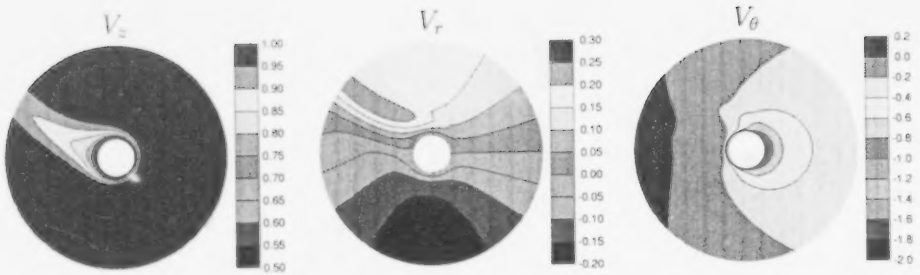

Figure A.52: *Shaft wake:* $R_e = 10^5$; $\Omega = 2.0$; $\beta = 10°$

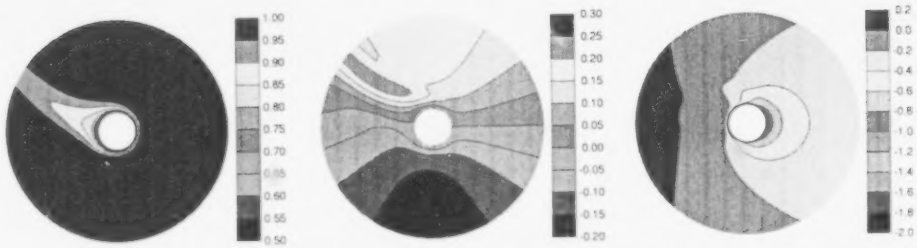

Figure A.53: *Shaft wake:* $R_e = 10^6$; $\Omega = 2.0$; $\beta = 10°$

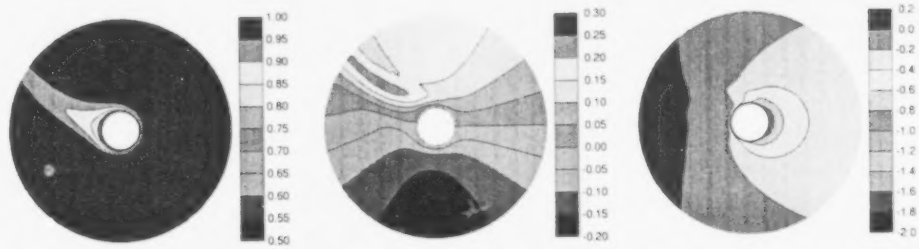

Figure A.54: *Shaft wake:* $R_e = 10^7$; $\Omega = 2.0$; $\beta = 10°$

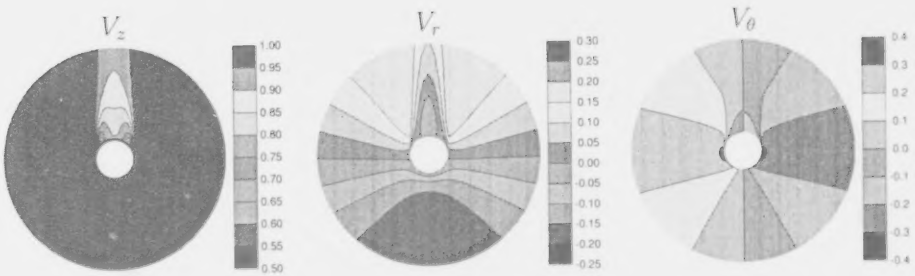

Figure A.55: *Shaft wake:* $R_e = 10^5$; $\Omega = 0.0$; $\beta = 12^\circ$

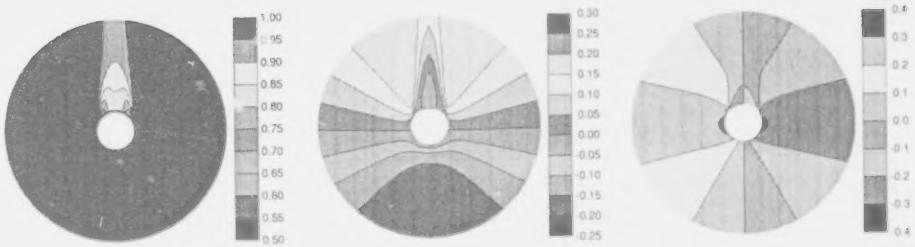

Figure A.56: *Shaft wake:* $R_e = 10^6$; $\Omega = 0.0$; $\beta = 12^\circ$

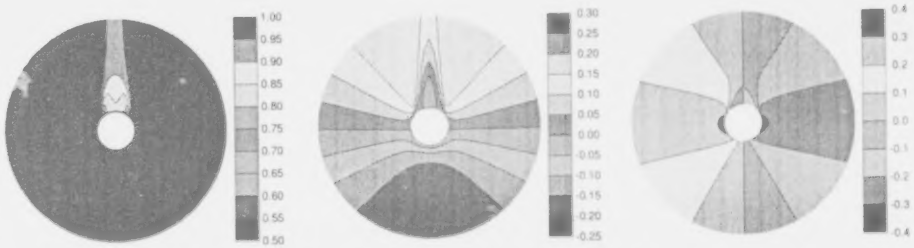

Figure A.57: *Shaft wake:* $R_e = 10^7$; $\Omega = 0.0$; $\beta = 12^\circ$

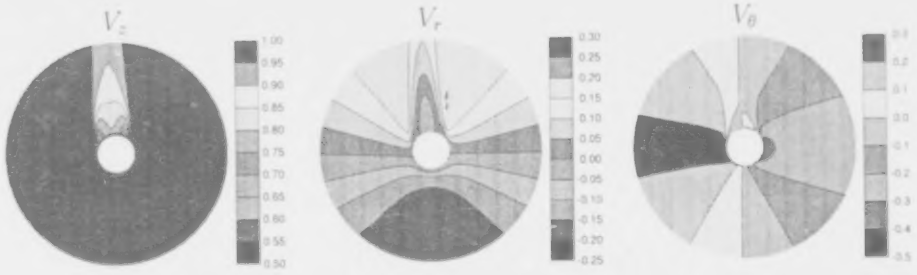

Figure A.58: *Shaft wake:* $R_e = 10^5$; $\Omega = 0.1$; $\beta = 12°$

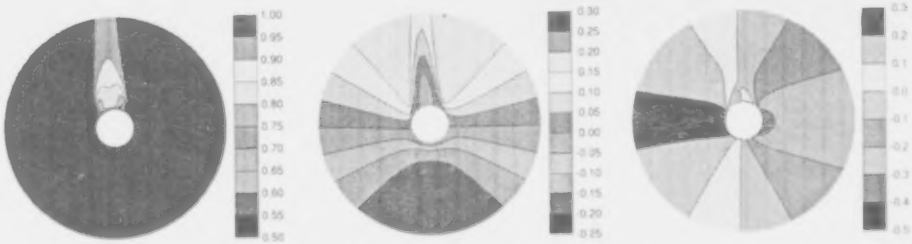

Figure A.59: *Shaft wake:* $R_e = 10^6$; $\Omega = 0.1$; $\beta = 12°$

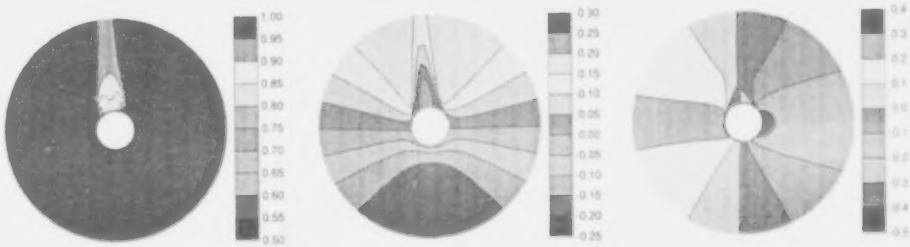

Figure A.60: *Shaft wake:* $R_e = 10^7$; $\Omega = 0.1$; $\beta = 12°$

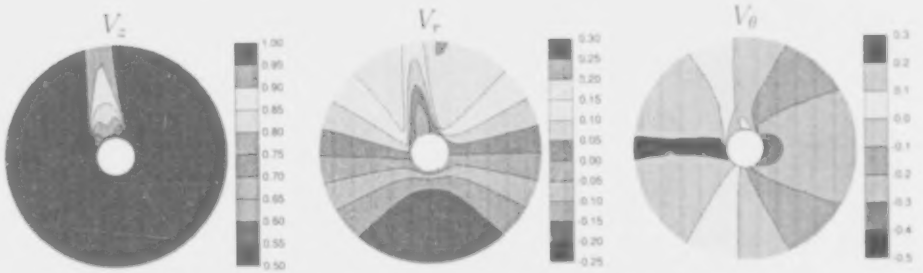

Figure A.61: *Shaft wake:* $R_e = 10^5$; $\Omega = 0.2$; $\beta = 12^\circ$

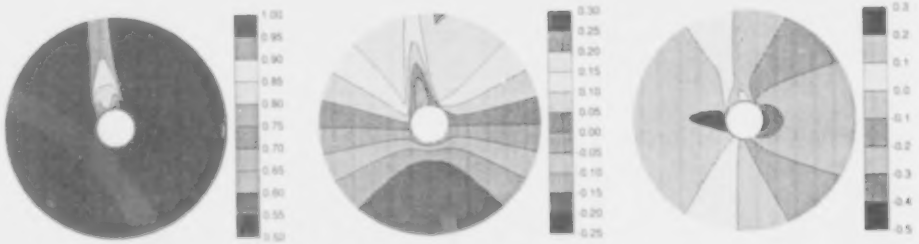

Figure A.62: *Shaft wake:* $R_e = 10^6$; $\Omega = 0.2$; $\beta = 12^\circ$

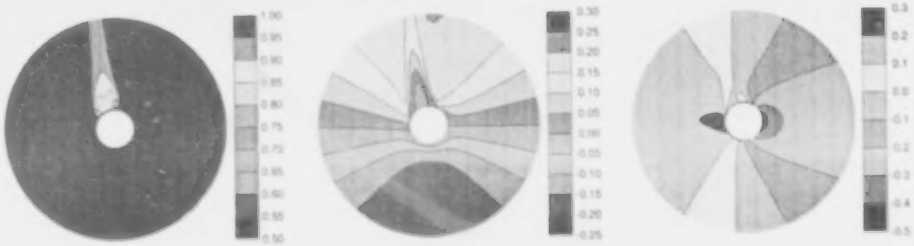

Figure A.63: *Shaft wake:* $R_e = 10^7$; $\Omega = 0.2$; $\beta = 12^\circ$

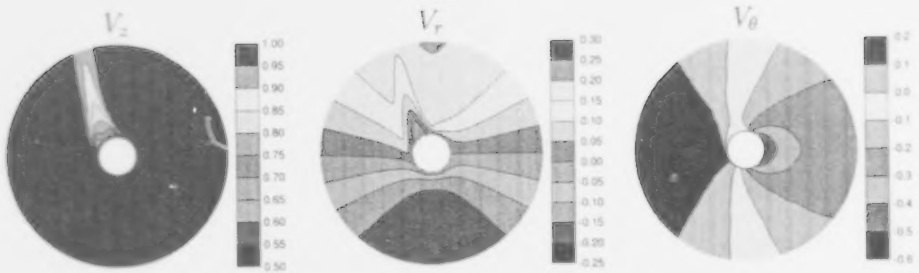

Figure A.64: *Shaft wake:* $R_e = 10^5$; $\Omega = 0.4$; $\beta = 12°$

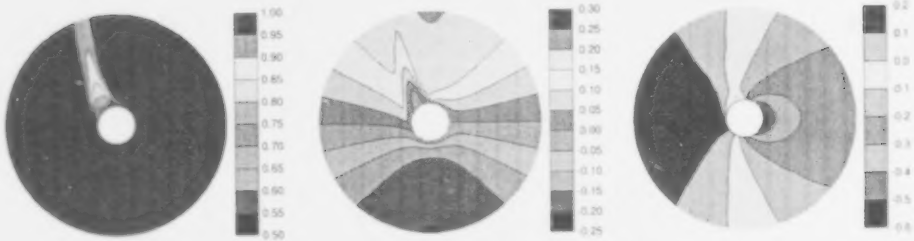

Figure A.65: *Shaft wake:* $R_e = 10^6$; $\Omega = 0.4$; $\beta = 12°$

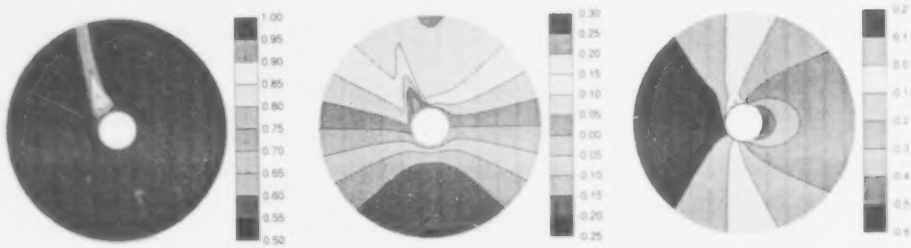

Figure A.66: *Shaft wake:* $R_e = 10^7$; $\Omega = 0.4$; $\beta = 12°$

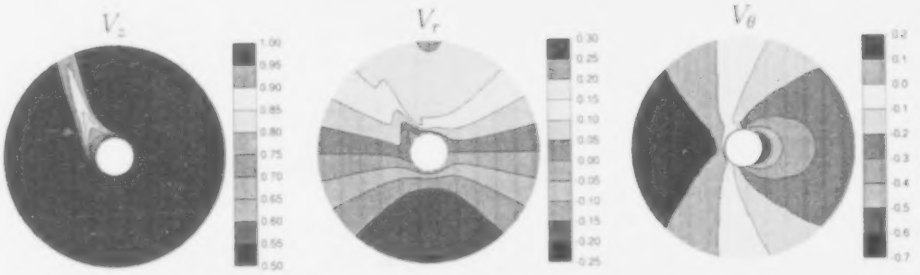

Figure A.67: *Shaft wake:* $R_e = 10^5$; $\Omega = 0.6$; $\beta = 12°$

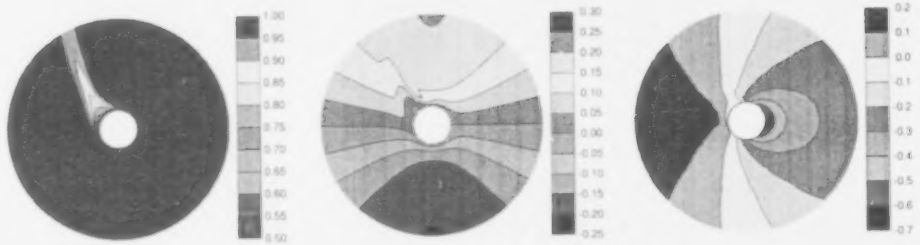

Figure A.68: *Shaft wake:* $R_e = 10^6$; $\Omega = 0.6$; $\beta = 12°$

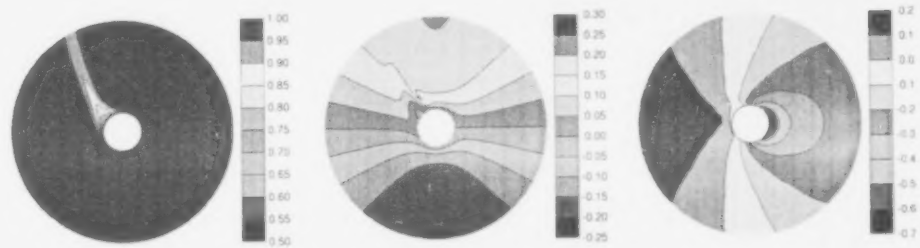

Figure A.69: *Shaft wake:* $R_e = 10^7$; $\Omega = 0.6$; $\beta = 12°$

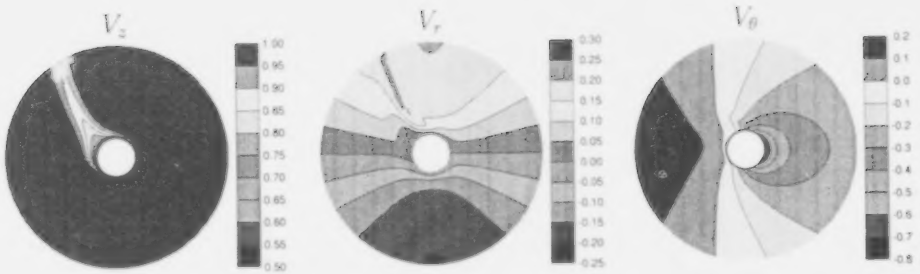

Figure A.70: *Shaft wake:* $R_e = 10^5$; $\Omega = 0.8$; $\beta = 12^\circ$

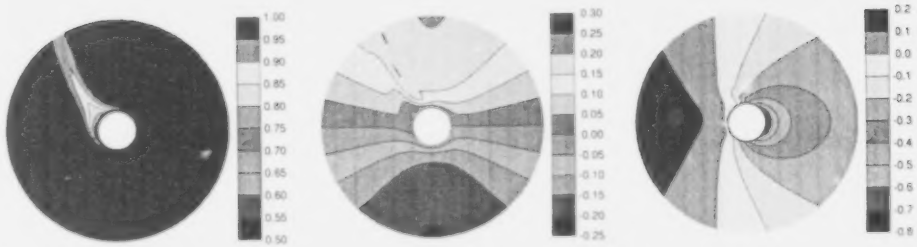

Figure A.71: *Shaft wake:* $R_e = 10^6$; $\Omega = 0.8$; $\beta = 12^\circ$

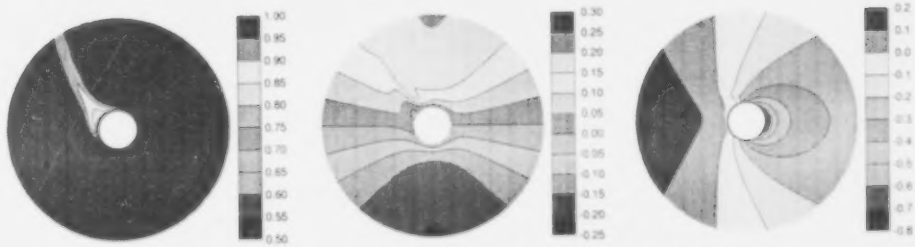

Figure A.72: *Shaft wake:* $R_e = 10^7$; $\Omega = 0.8$; $\beta = 12^\circ$

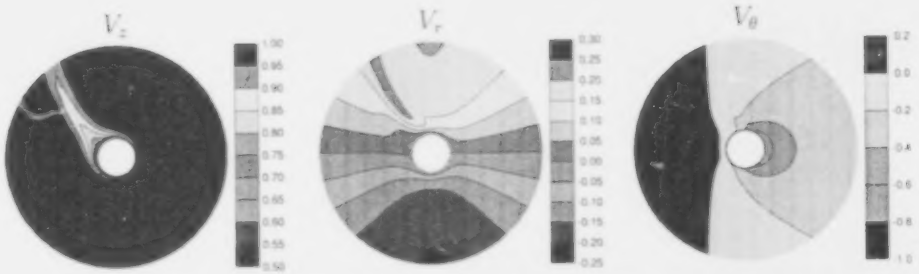

Figure A.73: *Shaft wake:* $R_e = 10^5$; $\Omega = 1.0$; $\beta = 12°$

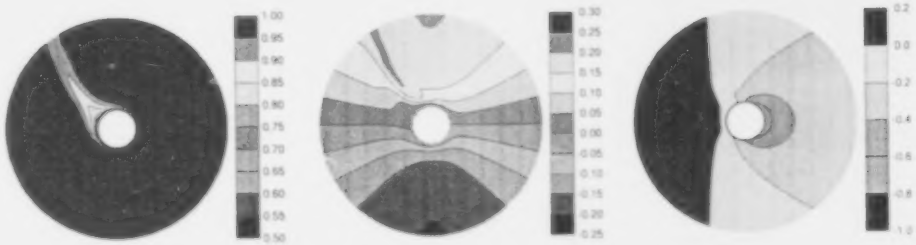

Figure A.74: *Shaft wake:* $R_e = 10^6$; $\Omega = 1.0$; $\beta = 12°$

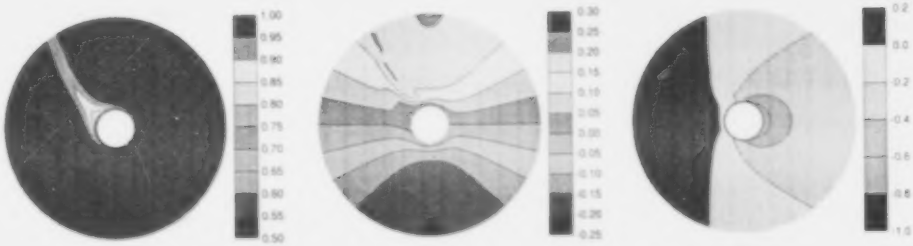

Figure A.75: *Shaft wake:* $R_e = 10^7$; $\Omega = 1.0$; $\beta = 12°$

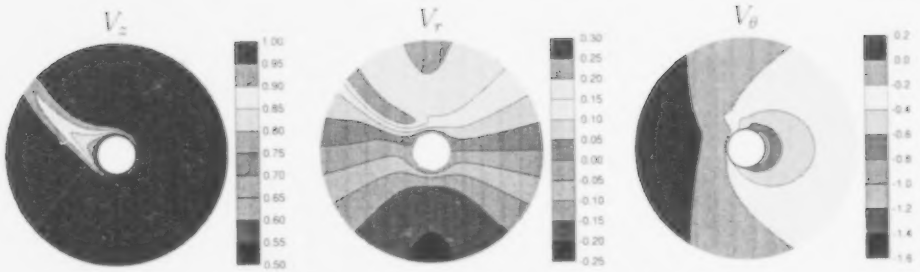

Figure A.76: *Shaft wake:* $R_e = 10^5$; $\Omega = 1.5$; $\beta = 12°$

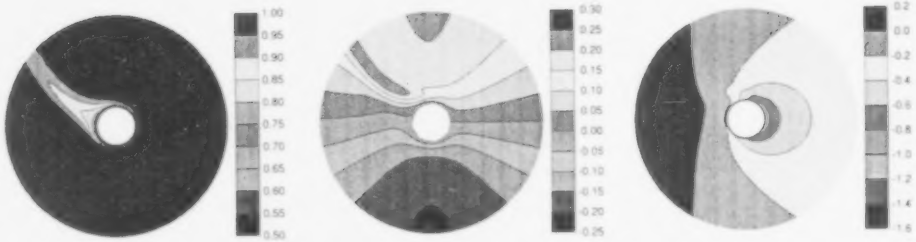

Figure A.77: *Shaft wake:* $R_e = 10^6$; $\Omega = 1.5$; $\beta = 12°$

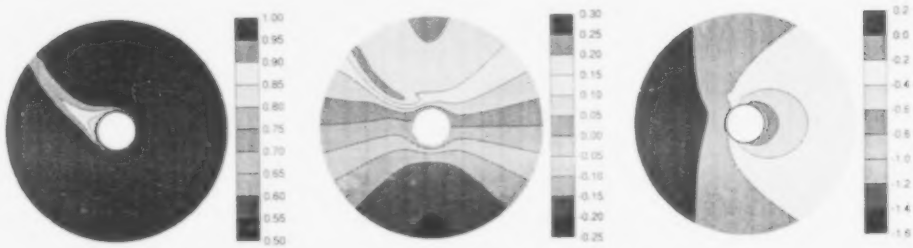

Figure A.78: *Shaft wake:* $R_e = 10^7$; $\Omega = 1.5$; $\beta = 12°$

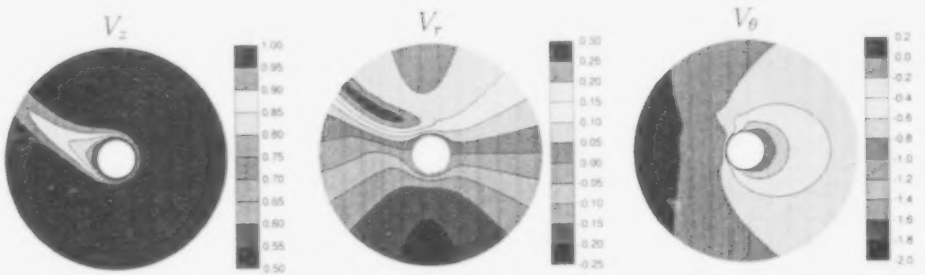

Figure A.79: *Shaft wake:* $R_e = 10^5$; $\Omega = 2.0$; $\beta = 12°$

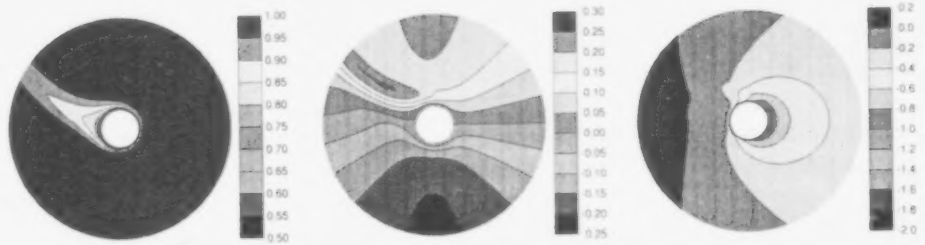

Figure A.80: *Shaft wake:* $R_e = 10^6$; $\Omega = 2.0$; $\beta = 12°$

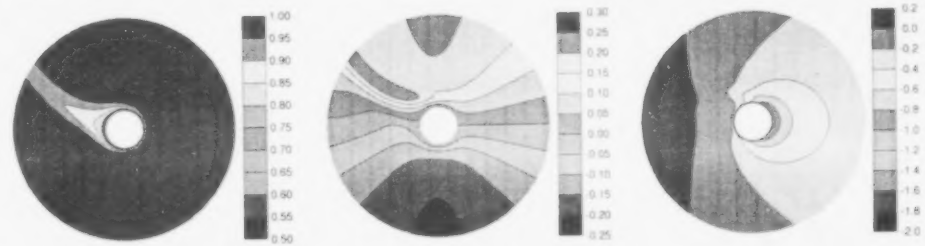

Figure A.81: *Shaft wake:* $R_e = 10^7$; $\Omega = 2.0$; $\beta = 12°$

Notation

β	Shaft inclination.
$\gamma(r)$	Circulation coefficient for a line of constant radius r.
θ	Angular position around the shaft.
$\kappa(r)$	Circulation around a line of constant radius r.
ν	Kinematic viscosity.
$\tilde{\nu}$	Spalart-Allmaras viscosity.
ν_t	Turbulent kinematic viscosity.
ρ	Fluid density.
ω	Angular velocity of the shaft; also vorticity in the Spalart-Allmaras turbulence model.
Ω	Shaft rotation parameter.
C_F	Side force coefficient.
D	Shaft diameter.
N_θ	Number of points circumferentially in the grid.
N_r	Number of points radially in the grid.
p	Pressure.
r	Distance from the axis of the shaft.
R_e	Reynolds number.
R_o	Radius if the outer boundary of the grid.
R_s	Radius of the shaft.
R_p	Radius of the propeller.
u	Horizontal component of the velocity.
v	Vertical component of the velocity.
V_∞	Speed of the flow far from the shaft.

v_θ	Circumferential component of the velocity.
V_c	Speed of the cross-flow.
v_r	Radial component of the velocity.
w	Axial component of the velocity.
x	Horizontal component of position.
y	Vertical component of position.

Distribution list

CANADA

Internal

1 Author

5 Library

Department of National Defence

National Defence Headquarters
MGen. George R. Pearkes Bldg.
101 Colonel By Drive
Ottawa, Ontario
K1A OK2

1 DRDKIM

2 DMSS 2

Others

2 Canada Institute for Scientific and Technical Information
Library Serials Acquisitions
National Research Council Canada
Ottawa, Ontario
K1A OS2

2 Canadian Acquisitions Division
National Library of Canada
395 Wellington Street
Ottawa, Ontario
K1A ON4
Attn: Government Documents

1 Director-General
Institute for Marine Dynamics
National Research Council of Canada
P.O. Box 12093, Station A
St. John's, Newfoundland
A1B 3T5

1 Director-General
Institute for Aerospace Research
National Research Council of Canada
Building M-13A
Ottawa, Ontario
K1A OR6

1 Transport Development Centre
Transport Canada
6th Floor
800 Rene Levesque Blvd, West
Montreal, Que.
H3B 1X9
Attn: Marine R&D Coordinator

1 Canadian Coast Guard
Ship Safety Branch
Canada Building, 11th Floor
344 Slater Street
Ottawa, Ontario
K1A 0N7
Att: Chief, Design and Construction

MOUs

12 Canadian Project Officer ABCA-02-01 (C/SCI. DRDC Atlantic – paper copies only)

29 total

DOCUMENT CONTROL DATA

(Security classification of title, body of abstract and indexing annotation must be entered when document is classified)

1. ORIGINATOR (the name and address of the organization preparing the document. Organizations for whom the document was prepared, e.g. Centre sponsoring a contractor's report, or tasking agency, are entered in section 8.)

Defence R&D Canada – Atlantic
PO Box 1012, Dartmouth, NS, Canada B2Y 3Z7

2. SECURITY CLASSIFICATION (overall security classification of the document including special warning terms if applicable)

UNCLASSIFIED

3. TITLE (the complete document title as indicated on the title page. Its classification should be indicated by the appropriate abbreviation (S,C,R or U) in parentheses after the title.)

The flow past infinite rotating cylinders at small inclinations

4. AUTHORS (Last name, first name, middle initial. If military, show rank, e.g. Doe, Maj. John E.)

Hally, D.

5. DATE OF PUBLICATION (month and year of publication of document)

January 2005

6a. NO. OF PAGES (total containing information. Include Annexes, Appendices, etc).

63

6b. NO. OF REFS (total cited in document)

6

7. DESCRIPTIVE NOTES (the category of the document, e.g. technical report, technical note or memorandum. If appropriate, enter the type of report, e.g. interim, progress, summary, annual or final. Give the inclusive dates when a specific reporting period is covered)

Technical Memorandum

8. SPONSORING ACTIVITY (the name of the department project office or laboratory sponsoring the research and development. Include address).

Defence R&D Canada – Atlantic
PO Box 1012, Dartmouth, NS, Canada B2Y 3Z7

9a. PROJECT OR GRANT NO. (if appropriate, the applicable research and development project or grant number under which the document was written. Specify whether project or grant).

Project 11cj18

9b. CONTRACT NO. (if appropriate, the applicable number under which the document was written).

10a. ORIGINATOR'S DOCUMENT NUMBER (the official document number by which the document is identified by the originating activity. This number must be unique.)

DRDC Atlantic TM 2004-274

10b. OTHER DOCUMENT NOs. (Any other numbers which may be assigned this document either by the originator or by the sponsor.)

11. DOCUMENT AVAILABILITY (any limitations on further dissemination of the document, other than those imposed by security classification)

(X) Unlimited distribution
( ) Defence departments and defence contractors; further distribution only as approved
( ) Defence departments and Canadian defence contractors; further distribution only as approved
( ) Government departments and agencies; further distribution only as approved
( ) Defence departments; further distribution only as approved
( ) Other (please specify):

12. DOCUMENT ANNOUNCEMENT (any limitation to the bibliographic announcement of this document. This will normally correspond to the Document Availability (11). However, where further distribution beyond the audience specified in (11) is possible, a wider announcement audience may be selected).

13. ABSTRACT (a brief and factual summary of the document. It may also appear elsewhere in the body of the document itself. It is highly desirable that the abstract of classified documents be unclassified. Each paragraph of the abstract shall begin with an indication of the security classification of the information in the paragraph (unless the document itself is unclassified) represented as (S), (C), (R), or (U). It is not necessary to include here abstracts in both official languages unless the text is bilingual).

In order to understand the effects of propeller shaft rotation on the flow into the propellers of a twin-screw ship, the DRDC Atlantic flow solver TRANSOM was used to calculate the flow around infinitely long rotating inclined cylinders at different Reynolds numbers.

The flow was solved at flow inclinations of $8°$, $10°$ and $12°$, at Reynolds numbers of 10^5, 10^6 and 10^7 based on shaft diameter, and at nine different rotation rates. The velocity fields for all 81 cases are displayed and the primary flow features and their dependence on shaft inclination, Reynolds number and rotation rate are discussed.

14. KEYWORDS, DESCRIPTORS or IDENTIFIERS (technically meaningful terms or short phrases that characterize a document and could be helpful in cataloguing the document. They should be selected so that no security classification is required. Identifiers, such as equipment model designation, trade name, military project code name, geographic location may also be included. If possible keywords should be selected from a published thesaurus, e.g. Thesaurus of Engineering and Scientific Terms (TEST) and that thesaurus-identified. If it not possible to select indexing terms which are Unclassified, the classification of each should be indicated as with the title).

Fluid flow
Computational fluid dynamics
Propeller shafts
Spalart-Allmaras turbulence model
TRANSOM